

A Submillimeter Perspective on the GOODS Fields (SUPER GOODS). V. Deep 450 μ m Imaging

A. J. BARGER,^{1,2,3} L. L. COWIE,³ A. H. BLAIR,¹ AND L. H. JONES^{1,4}

¹Department of Astronomy, University of Wisconsin-Madison, 475 N. Charter Street, Madison, WI 53706, USA

²Department of Physics and Astronomy, University of Hawaii, 2505 Correa Road, Honolulu, HI 96822, USA

³Institute for Astronomy, University of Hawaii, 2680 Woodlawn Drive, Honolulu, HI 96822, USA

⁴Space Telescope Science Institute, 3700 San Martin Drive, Baltimore, MD 21218, USA

ABSTRACT

We present deep SCUBA-2 450 μ m imaging of the two GOODS fields, achieving a central rms of 1.14 mJy for the GOODS-N and 1.86 mJy for the GOODS-S. For each field, we give a catalog of $> 4\sigma$ detections (79 and 16 sources, respectively). We construct the 450 μ m number counts, finding excellent agreement with others from the literature. We match the 450 μ m sources to 20 cm data (both fields) and ALMA 870 μ m data (GOODS-S) to gauge the accuracy of the 450 μ m positions. We use the extensive redshift information available on the fields to test how well redshift can be estimated from simple flux ratios (450 μ m/850 μ m and 20 cm/850 μ m), finding tight correlations. We provide a catalog of candidate high-redshift submillimeter galaxies. We look for evolution in dust temperature with redshift by fitting the spectral energy distributions of the sources, but we do not find any significant redshift evolution after accounting for the far-infrared luminosity. We do not find evidence for 450 μ m selection picking out warmer sources than 850 μ m selection. We find that a 450 μ m selected sample only adds low-redshift ($z < 1.5$) galaxies beyond an 850 μ m sample.

Keywords: cosmology: observations — galaxies: distances and redshifts — galaxies: evolution — galaxies: starburst

1. INTRODUCTION

Submillimeter galaxies (SMGs) are some of the most powerfully star-forming galaxies in the universe. The use of deep imaging with the Submillimeter Common-User Bolometer Array (SCUBA; Holland et al. 1999) on the 15 m James Clerk Maxwell Telescope (JCMT) brought these distant, dusty, and ultraluminous galaxies into view for the first time (e.g., Smail et al. 1997; Barger et al. 1998; Hughes et al. 1998; Eales et al. 1999). Their star formation rates (SFRs) are in excess of $500 M_{\odot} \text{ yr}^{-1}$. They are significant contributors to the star formation history out to redshifts of at least 5 (e.g., Barger et al. 2000, 2012, 2014; Chapman et al. 2005; Wardlow et al. 2011; Casey et al. 2013; Swinbank et al. 2014; Cowie et al. 2017) and hence critical for understanding galaxy evolution.

SCUBA was replaced by the second-generation camera SCUBA-2 (Holland et al. 2013), which vastly improved ground-based submillimeter astronomy by achieving a field-of-view of 50 arcmin², 16 times larger than its predecessor. It is the preeminent instrument for obtaining the wide-field maps required to identify large numbers of SMGs. There is currently no other submillimeter instrument that can match its mapping speed. SCUBA-2 observes simultaneously at 450 μ m and 850 μ m, but useful 450 μ m observations are possible only during the small fraction ($\sim 15\%$) of nights on

Mauna Kea when the precipitable water vapor is exceptionally low.

The natural limit of single-dish submillimeter observations is the depth at which confusion, which refers to the blending of sources or where the noise is dominated by unresolved contributions from fainter sources, becomes important. At 850 μ m, the JCMT has a resolution of 14'' FWHM, which allows the construction of very large and uniform samples of SMGs brighter than the ~ 1.65 mJy (4σ) confusion limit (Cowie et al. 2017). However, it also results in source blending and unresolved galaxies. Targeted follow-up observations with submillimeter interferometers, such as the Atacama Large Millimeter/submillimeter Array (ALMA), are able to provide accurate positions, to resolve the sources, and to determine multiplicity, but their small fields-of-view mean interferometers are too costly for the initial selection of large sample of SMGs.

An alternative way to get higher resolution is to go to shorter wavelengths. At 450 μ m, the JCMT has a resolution of 7''.5 FWHM. (Note that this is a considerably higher resolution than the $\sim 35''$ FWHM of *Herschel* at 500 μ m.) These higher resolution data (i) substantially reduce the confusion limit, thereby allowing the more typical sources that contribute the bulk of the submillimeter EBL to be found; (ii) make it possible to measure fluxes at rest wavelengths close to the peak

of the blackbody distribution in the far-infrared (FIR); (iii) allow measurements of the FIR spectral energy distributions (SEDs), when combined with the 850 μm data and with *Herschel* and *Spitzer* data for isolated, brighter sources; and (iv) allow much more accurate positions to be obtained for the sources than is possible at 850 μm . With this positional accuracy, we can begin to identify optical/near-infrared (NIR) counterparts reliably, even without follow-up interferometric observations.

The deepest blank-field 450 μm image is from the SCUBA-2 Ultra Deep Imaging EAO Survey (STUDIES; e.g., Wang et al. 2017; Lim et al. 2020), a multiyear JCMT Large Program that uses the CV DAISY scan pattern (Holland et al. 2013) and aims to reach the confusion limit at 450 μm in the COSMOS field. Lim et al. (2020) report a central rms of 0.75 mJy at 450 μm for their 184 hr of on-sky observations. They combine STUDIES with existing data from Casey et al. (2013; Lim et al. quote 3.6 mJy for 38 hr; this uses the wider PONG-900 scan pattern) and Geach et al. (2013; Lim et al. quote 0.95 mJy for 150 hr in the deepest region; this is a mosaic of two CV DAISY maps with some overlap). The rms of the combined datasets in the deepest region is 0.65 mJy (Lim et al. 2020). Another field with deep 450 μm data is the SCUBA-2 Cosmology Legacy Survey (S2CLS) Extended Groth Strip or EGS (this uses the CV DAISY scan pattern), for which Zavala et al. (2017) quote a central rms of 1.2 mJy at 450 μm .

In this paper, we focus on analyzing our deep SCUBA-2 450 μm observations of both GOODS fields. We have been observing the GOODS fields for many years, most recently through our Submillimeter PERspective on the GOODS fields (SUPER GOODS) program. We chose these fields, because they are the most richly observed fields on the sky, with 4 optical bands (B through z) from the *HST*/ACS GOODS survey (Giavalisco et al. 2004) and two NIR bands from the *HST*/WFC3 CANDELS survey (Grogin et al. 2011; Koekemoer et al. 2011). The *Spitzer*/MIPS 70 μm survey (and associated 24 and 160 μm data) and the deep *Herschel* FIR surveys are also among the deepest ever taken and provide sufficient sensitivity to constrain the dust SEDs of the SMGs (e.g., Oliver et al. 2010; Lutz et al. 2011; Barger et al. 2012, 2014; Cowie et al. 2017, 2018). The GOODS-N has ultradeep 20 cm observations providing an rms noise in the field center of 2.2 μJy (Owen 2018), reflecting the power of the upgraded Karl G. Jansky Very Large Array (VLA). Meanwhile, the GOODS-S has VLA 20 cm observations that reach a best rms sensitivity of 6 μJy (Miller et al. 2013). Finally, both fields have spectroscopic observations for many thousands of galaxies (e.g., Barger, Cowie, & Wang 2008; Popesso et al. 2009; Balestra et al. 2010; Barger et al. 2019 and references therein). *Chandra* obtained a 7 Ms X-ray image of the *Chandra* Deep Field-South (CDF-S; Luo et al. 2017), which is by far the deepest X-ray image ever taken, followed only by the 2 Ms *Chandra* Deep Field-

North (CDF-N; Alexander et al. 2003). Our SCUBA-2 observations cover the most sensitive regions of the *Chandra* images and almost the entire GOODS areas.

This is the fifth paper in our SUPER GOODS series. In the first two papers in the series (Cowie et al. 2017 and Barger et al. 2017), we analyzed the SCUBA-2 850 μm observations of the GOODS-N/CANDELS/CDF-N, complemented with targeted Submillimeter Array (SMA) interferometry, VLA interferometry, *Herschel* imaging, and spectroscopy. In the next two papers in the series (Cowie et al. 2018 and Barger et al. 2019), we analyzed the SCUBA-2 850 μm observations of the GOODS-S/CANDELS/CDF-S, complemented with targeted ALMA 870 μm interferometry, *Herschel* imaging, and spectroscopy.

In Section 2, we describe our SCUBA-2 observations and data reduction, determine our 450 μm selected samples, and present the primary ancillary data used in this paper. In Section 3, we construct the 450 μm number counts. In Section 4, we use combinations of the 450 μm , 850 μm , and 20 cm bands to identify candidate high-redshift galaxies. In Section 5, we construct SEDs from our multiwavelength data and fit them with the publicly available Bayesian energy-balance SED-fitting code MAGPHYS (da Cunha et al. 2015) to obtain SFRs and dust properties. We also construct gray body fits for comparison. In Section 6, we examine the MAGPHYS SFRs and FIR luminosities for galaxies with either a spectroscopic or photometric redshift $z > 1$. In Section 7, we discuss the redshift distribution of the 450 μm selected sample and the dependence of dust temperature on redshift and FIR luminosity. In Section 8, we summarize our results.

2. DATA

2.1. SCUBA-2 Observations

In Cowie et al. (2017, 2018), we presented SCUBA-2 850 μm catalogs ($> 4\sigma$) of the GOODS-N (Cowie et al. 2017’s Table 5) and GOODS-S (Cowie et al. 2018’s Table 2; this just covered the central 100 arcmin^2 region) through mid-2016 and through early 2017, respectively. We also presented a SCUBA-2 450 μm catalog ($> 4\sigma$) of the GOODS-N (Cowie et al. 2017’s Table 6),

We have continued to deepen our observations. To obtain maximum depth in the central region, we used the CV DAISY scan pattern, whose field size is 5.5’ in radius (by this radius, the noise is twice the central noise). To cover the outer regions to find brighter but rarer sources, we used the larger field PONG-900 scan pattern, whose field size is 10.5’ in radius (by this radius, the noise is twice the central noise).

We summarize the total weather band 1 ($\tau_{225 \text{ GHz}} < 0.05$) and weather band 2 ($0.05 < \tau_{225 \text{ GHz}} < 0.08$) SCUBA-2 observations in Table 1. These are the only weather conditions under which 450 μm observations can be usefully obtained. The GOODS-N observations have a central rms of 1.14 mJy at 450 μm , and the

Table 1. SCUBA-2 Observations

Field	Weather	Scan	Exposure
		Band	Pattern
GOODS-N	1	CV Daisy	140.84
	1	PONG-900	20.01
	2	CV Daisy	27.79
	2	PONG-900	16.37
GOODS-S	1	CV Daisy	50.12
	1	PONG-900	16.20
	2	CV Daisy	35.63
	2	PONG-900	8.70

GOODS-S 1.86 mJy. These values do not include confusion noise.

Our reduction procedures follow Chen et al. (2013b) and are described in detail in Cowie et al. (2017). The galaxies are expected to appear as unresolved sources at the 7''.5 resolution of the JCMT at 450 μ m. We therefore applied a matched filter to our maps, which provides a maximum likelihood estimate of the source strength for unresolved sources (e.g., Serjeant et al. 2003). Each matched-filter image has a PSF with a Mexican hat shape and an FWHM corresponding to the telescope resolution.

For both fields, we chose sources in an area where the noise is less than 3.75 mJy (roughly 3 times the central noise for the GOODS-N and 2 times for the GOODS-S). For the GOODS-N, this corresponds to an area of 175 arcmin², and for the GOODS-S, 48 arcmin². As described in Cowie et al. (2017), we extracted point sources by identifying the peak signal-to-noise (S/N) pixel, subtracting this peak pixel and its surrounding areas using the PSF scaled and centered on the value and position of that pixel, and then searching for the next S/N peak. We iterated this process until we reached a S/N of 3.5. We then limited the sample to the sources with a S/N above 4, giving 79 450 μ m sources in the GOODS-N and 16 in the GOODS-S. Our S/N choice of $> 4\sigma$ should minimize the number of spurious sources in our catalogs to $\leq 5\%$ (e.g., Chen et al. 2013a; Casey et al. 2013).

The reason for the iterative process described above is to remove contamination by brighter sources before we identify fainter sources and measure their fluxes. While critical for the 850 μ m data, it is somewhat less necessary for the 450 μ m data due to its higher resolution and shallower depth. However, we still followed the procedure.

We matched our 450 μ m sources to $> 4\sigma$ 850 μ m sources within 4''. In cases where there was no 850 μ m match, we measured the 850 μ m flux for the source at the 450 μ m position. For these measurements, we first

removed all of the 450 μ m sources with an 850 μ m source match from the 850 μ m matched-filter SCUBA-2 images using a PSF based on the observed calibrators. This left residual images from which we measured the 850 μ m fluxes (whether positive or negative) and statistical uncertainties at the 450 μ m positions. This procedure minimizes contamination by brighter 850 μ m sources in the field.

In Tables 2 and 3, we give the 450 μ m and 850 μ m fluxes for, respectively, the GOODS-N and GOODS-S $> 4\sigma$ 450 μ m samples. In the GOODS-N, there are two pairs of 450 μ m galaxies that are blended at 850 μ m, and in the GOODS-S, there is one. In these cases, we have assigned the 850 μ m flux measured at the 450 μ m source position of the brighter member of the pair to that member, and we have not assigned an 850 μ m flux to the fainter member of the pair (the fainter sources are labeled “blend” in the 850 μ m flux column in the tables, along with the source number of the brighter member of the pair).

Lim et al. (2020) estimated the fraction of sources in their 450 μ m sample that are also detected at 850 μ m by considering how many 850 μ m fluxes—all of which they measured at the 450 μ m source positions—are five times higher than their estimate of the confusion noise (0.42 mJy), namely 2.1 mJy. They found that 99 of their 256 sources satisfied this criterion. This can be thought of as them determining how many of their 450 μ m sources would be contained in a $> 5\sigma$ 850 μ m selected sample, which is a fairly low 38%. Using the same procedure, we find that 68 of our 92 sources (after excluding the three fainter members of the blends) have 850 μ m fluxes above 2.1 mJy, or a much higher 74%. This may reflect our slightly shallower 450 μ m sample: when the 450 μ m fluxes are brighter, then they are easier to detect in a confusion-limited 850 μ m image.

However, another approach to determining the overlap between samples is to take advantage of our ability to probe below the 850 μ m confusion limit with our predetermined 450 μ m sample. After excluding the three fainter members of the blends, all but 9 of our remaining 92 450 μ m sources are also detected at high significance ($> 4\sigma$) at 850 μ m. We show 850 μ m flux versus 450 μ m flux for the combined GOODS sample in Figure 1 with these 9 sources denoted by green squares. In order to quantify the level of contamination, we measured 850 μ m fluxes at randomized positions, finding that 7% of these measurements result in a $> 4\sigma$ 850 μ m measurement. Allowing for this contamination, we conclude that 82% of our 450 μ m sample is detected at $> 4\sigma$ at 850 μ m.

We also have two sources in the GOODS-N and one source in the GOODS-S whose optical/NIR photometry is contaminated by a neighboring star or galaxy. We label these “contam.” in the redshift column in the tables, since no redshifts could be determined for them.

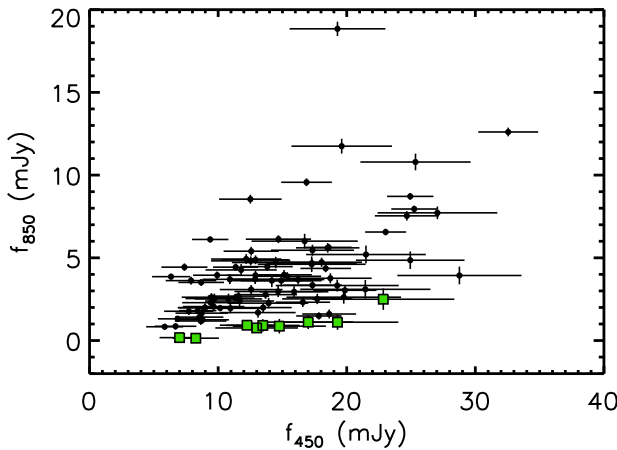


Figure 1. Based on the combined GOODS-N (Table 2) and GOODS-S (Table 3) samples, SCUBA-2 850 μm flux vs. SCUBA-2 450 μm flux with uncertainties on both quantities. The fainter members of the three blended 450 μm pairs have been excluded. The green squares show the 9 450 μm selected sources that are not also significantly ($> 4\sigma$) detected at 850 μm .

We will hereafter refer to the sample of 89 sources, after removal of the three fainter members of the blends and the three optical/NIR contaminated sources, as our *450 μm selected combined GOODS sample*.

2.2. VLA 20 cm Observations

The upgrade of the VLA greatly increased the sensitivity of the decimetric continuum observations that can be obtained. Here we use the extremely deep 20 cm image of the CDF-N field with a best rms sensitivity of 2.2 μJy (Owen 2018). The image covers a 40' diameter region with an effective resolution of 1''.8. The absolute radio positions are known to 0''.1 – 0''.2 rms. The highest sensitivity region, about 9' in radius, is closely matched to the full area of our SCUBA-2 survey and completely covers the deepest region of our map. There are 787 distinct $\geq 5\sigma$ radio sources within the 9' radius, excluding sources that appear to be parts of other sources. We used these data in analyzing the SCUBA-2 850 μm sources in Cowie et al. (2017) and Barger et al. (2017). For the small number of sources outside the Owen (2018) field, we used radio fluxes from Morrison et al. (2010).

We find that 73 of the 79 450 μm sources lie in the area covered by the Owen (2018) 20 cm observations. Of these, 63, or 86%, have 20 cm counterparts within 4''. If we reduce the match radius to 3'', then the number with 20 cm counterparts drops to 57. Following Cowie et al. (2017), we have included HDF850.1 (originally detected in the SCUBA map by Hughes et al. 1998; the galaxy's redshift of $z = 5.183$ was eventually measured from CO observations by Walter et al. 2012) in these numbers.

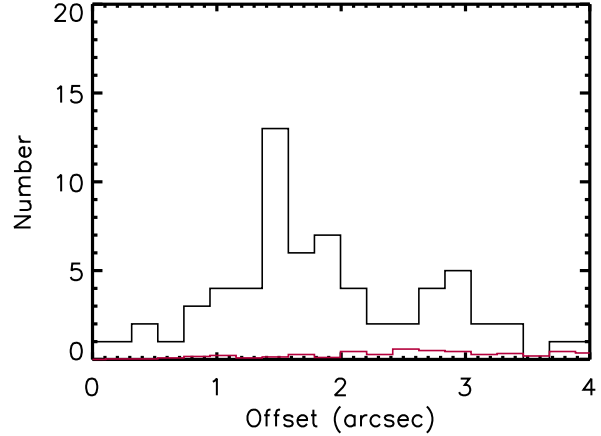


Figure 2. Offsets between the 65 SCUBA-2 450 μm centroid positions and the radio positions for counterparts within 4''. The mean offset is 2''.0, and the median offset is 1''.7. The red curve shows the histogram of offsets that would be expected between the positions of a random distribution of 450 μm sources and the radio positions for counterparts within 4'', based on 64 simulations.

It lies just below the Owen (2018) flux threshold and is offset from the radio position by 1''.8.

We checked the absolute astrometric pointing of the 450 μm map by comparing the positions of the 450 μm sources with radio counterparts with the radio positions. We found offsets of $-0''.76$ in R.A. and $-0''.33$ in Decl., which are small compared to the positional uncertainties of the 450 μm data. We applied these corrections to the 450 μm positions.

In Figure 2, we show the offsets of the radio counterparts. To compare with expectations for offsets between the radio sources and a random distribution of 450 μm sources, we generated 64 simulated 450 μm maps by removing the 79 true sources from the image and each time randomly populating this cleaned map with 79 sources with the same fluxes as the real sample. The red curve shows the offset results from the simulations. The number of random identifications only becomes comparable to the number of actual identifications above about 3''.5, showing that most of the closer identifications are real.

For the GOODS-S, we use the VLA 20 cm catalog of Miller et al. (2013) of the Extended CDF-S, which covers an area of about a third of a square degree and reaches a best rms sensitivity of 6 μJy . Their catalog contains 883 distinct radio sources. For this field, we do our absolute astrometric pointing check and offset calculation using the ALMA data (see Section 2.3).

2.3. ALMA 850 μm Observations of the GOODS-S

In the most sensitive 100 arcmin^2 area, all of the > 2.25 mJy SCUBA-2 850 μm sources ($> 4\sigma$) have been

observed with ALMA in band 7 (870 μm), together with a number of fainter SCUBA-2 sources. Details of these observations and their reductions may be found in Cowie et al. (2018). We restrict the area of the individual ALMA images to their FWHM radius of 8''.75. With this restriction, the ALMA images cover a (non-contiguous) total area of 7.2 arcmin². We used these data in analyzing the SCUBA-2 850 μm sources in Cowie et al. (2018) and Barger et al. (2019).

Note that some of the ALMA sources are off the 450 μm area that we use in this paper (see Section 2.1). Based on the mean offset of 11 isolated ALMA sources with 870 μm fluxes > 2.25 mJy from the nearest SCUBA-2 450 μm peak, we found an absolute astrometric offset of 1''.44 in R.A. and 1''.28 in Decl., which we applied to the SCUBA-2 450 μm positions in Table 3. This is well within the expected uncertainty in the absolute SCUBA-2 450 μm astrometry.

In Figure 3(a), we show the ALMA observed areas (gray circles) with the SCUBA-2 450 μm source positions overlaid (red squares). 13 of the 16 450 μm sources lie on an ALMA image. In Figure 3(b), we show the ALMA sources convolved with the SCUBA-2 850 μm PSF with the 450 μm source positions again overlaid (red squares). 12 of the 13 450 μm sources that lie on an ALMA image have an ALMA source counterpart within 4''; the remaining 450 μm source lies on the edge of an ALMA image, as noted in Table 3. In Figure 3(c), we show the 450 μm image with the ALMA > 2.25 mJy source positions overlaid (white squares). Some of the 450 μm sources do not correspond to the ALMA > 2.25 mJy sample, and some of the ALMA > 2.25 mJy sample do not have 450 μm counterparts at our current sensitivity level.

2.4. Optical/NIR Fluxes

The GOODS fields are defined by the deep *HST*/ACS optical imaging of Giavalisco et al. (2004). These fields are also covered by deep CANDELS *HST*/WFC3 ultraviolet/optical and infrared channel imaging (Grogin et al. 2011; Koekemoer et al. 2011), and there are *Spitzer*/IRAC observations from the GOODS *Spitzer* Legacy Program (PI: M. Dickinson) and from the SEDS and S-CANDELS surveys (Ashby et al. 2013, 2015).

In the GOODS-N, we used the CANDELS/SHARDS multiwavelength catalog of Barro et al. (2019) for our photometry, after identifying counterparts to our 450 μm selected sample using a 1'' search radius if there is an accurate position from the radio or the Submillimeter Array, and a 3'' search radius otherwise. 55 of the 79 sources lie within the Barro et al. area and have counterparts within 1''.

In the GOODS-S, we used the multiwavelength catalog of Guo et al. (2014) for our photometry, after identifying counterparts to our 450 μm selected sample using a 1'' search radius if there is an accurate position from the radio or ALMA, and a 3'' search radius otherwise.

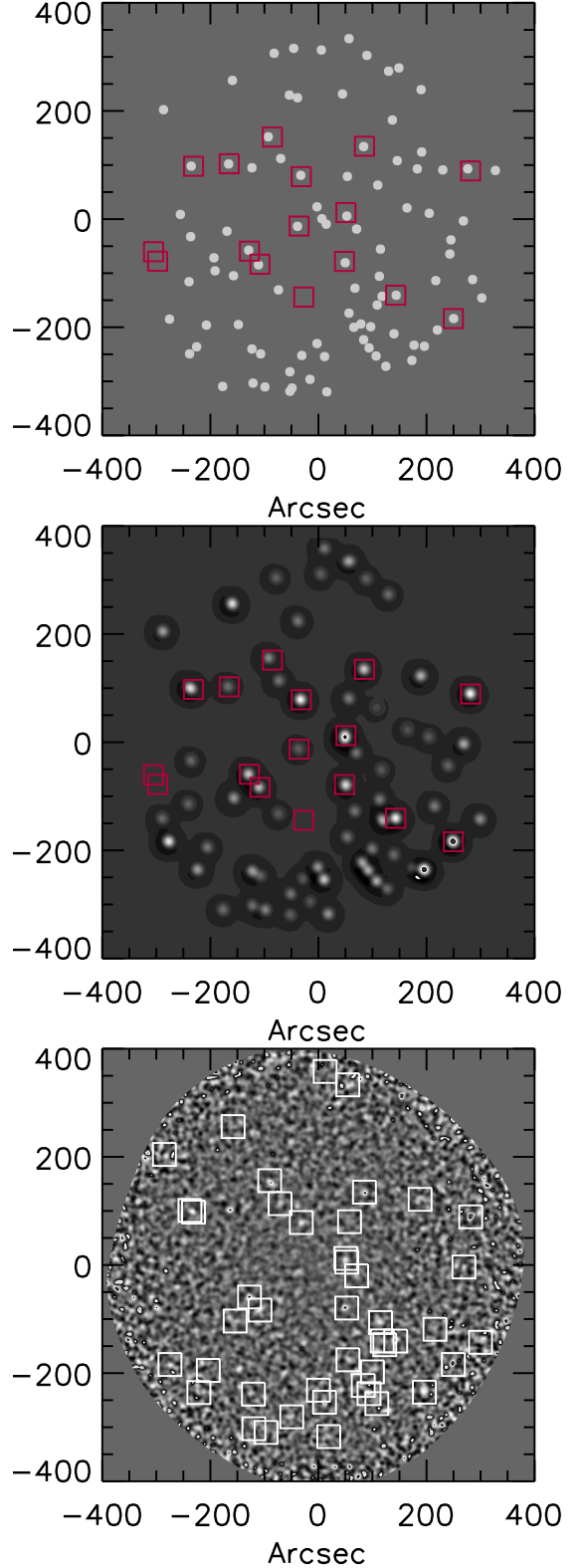


Figure 3. (a) ALMA observed areas and (b) ALMA sources convolved with SCUBA-2 850 μm PSF. The 450 μm source positions are overlaid in both panels (red squares). (c) 450 μm image with the ALMA > 2.25 mJy source positions overlaid (white squares). The images are centered at R.A. = 3^h32^m26^s, decl. = -27°48'17'', with the x-axis (y-axis) corresponding to offsets in R.A. (decl.) from this position.

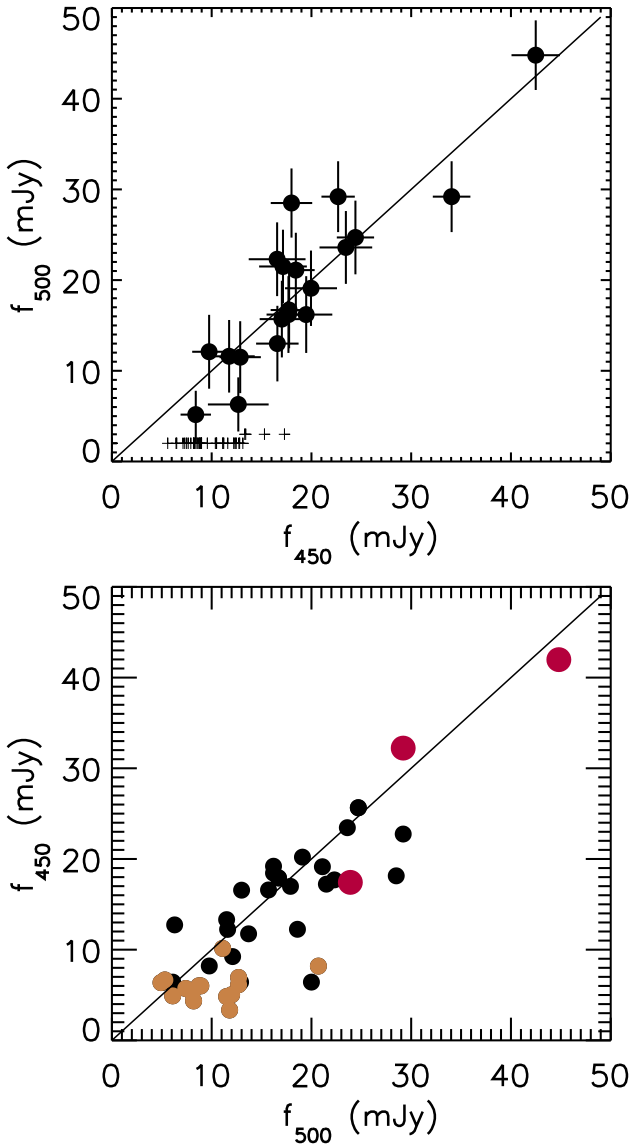


Figure 4. (a) *Herschel* 500 μm flux from the E11 GOODS-N catalog vs. SCUBA-2 450 μm flux from Table 2 for the 63 450 μm sources with noise < 2.8 mJy (twice the minimum noise). Black circles denote 450 μm sources with a 500 μm counterpart within 3.5'' of the 450 μm position. Plus signs show the remaining sources at the bottom (a slight vertical offset separates sources > 12 mJy from those < 12 mJy). For sources 1 and 6 in Table 2, each of which has a very nearby second source, we show the combined 450 μm flux. The plotted flux uncertainties are 1σ at both 450 μm and 500 μm . (b) SCUBA-2 450 μm flux vs. *Herschel* 500 μm flux for all sources in the E11 catalog that lie in the SCUBA-2 area with 450 μm noise < 2.8 mJy. Black circles show 500 μm sources with a 450 μm counterpart within 12'' of the 500 μm source position. Red circles show 500 μm sources with multiple 450 μm counterparts within 12'' of the 500 μm source; in these cases we use the combined 450 μm flux. Gold circles show 500 μm sources with no 450 μm counterparts in Table 2; in these cases, we measured the 450 μm fluxes directly from the image at the *Herschel* catalog positions.

All of the sources with accurate positions lie within the Guo et al. area and have counterparts within 1''.

2.5. MIR/FIR Fluxes

We used the catalogs of Magnelli et al. (2011) and Elbaz et al. (2011; hereafter, E11), respectively, to obtain the *Spitzer*/MIPS 24 μm fluxes for the GOODS-N and GOODS-S fields. These catalogs were constructed using the deep 24 μm MIPS images from the *Spitzer* GOODS Legacy program (PI: M. Dickinson). We used the catalogs of Magnelli et al. (2013) and E11, respectively, to obtain the *Herschel*/PACS 100 μm and 160 μm fluxes for the GOODS-N and GOODS-S fields. Magnelli et al. (2013) constructed the GOODS-N catalog using the combined data sets of the PACS Evolutionary Probe (PEP; Lutz et al. 2011) guaranteed time key program and the GOODS-*Herschel* (E11) open time key program, while E11 constructed the GOODS-S catalog using the GOODS-*Herschel* program data. We also used the wider area *Herschel*/SPIRE 250 μm , 350 μm , and 500 μm catalogs from E11 for both fields.

E11 and Magnelli et al. (2013) both used 24 μm priors to deblend the *Herschel* data when constructing their catalogs. They provide a detailed discussion of the robustness of the 24 μm priors in deblending the longer wavelength data. They also provide flags to assess whether sources are contaminated by nearby brighter sources.

We cross-identified the 450 μm samples with the > 20 μJy 24 μm sources, which are what E11 used as priors in measuring the *Herschel*/PACS 100 μm fluxes. For the unmatched sources, we measured the fluxes ourselves in the 24 μm images at the 450 μm positions using a 3'' diameter aperture. We aperture corrected these 24 μm fluxes using an average correction inferred from the matched sources. We then measured fluxes in the longer wavelength data using matched-filter images, after first removing the sources in the Magnelli et al. (2011) and E11 catalogs from the images.

We examined the relative calibration of the SCUBA-2 450 μm data versus the *Herschel* 500 μm data using the GOODS-N data. In Figure 4(a), we plot 500 μm flux from the E11 catalog versus 450 μm flux from Table 2 for the 63 sources with noise < 2.8 mJy. Above a 450 μm flux of 12 mJy, there are 19 sources in the figure, all but 4 of which are detected at 500 μm . Three of the non-detections at 500 μm (non-detections are shown with plus signs in the figure) have measured 350 μm fluxes, so the 500 μm fluxes are simply too faint for the catalog. The fourth (source 26 in Table 2) appears to have had its 500 μm flux allocated by E11 to a 24 μm source that is a neighbor to the correct 24 μm counterpart.

For these bright sources, the median 450 μm to 500 μm flux ratio is 1.00, and the median 450 μm to 350 μm flux ratio is 0.68. Interpolation of the *Herschel* data gives a median SCUBA-2 450 μm to interpolated *Herschel* 450 μm flux ratio of 0.90, so the SCUBA-2 data

are slightly fainter on average than the *Herschel* data. However, the difference is well within the calibration uncertainty in both data sets. There is also uncertainty due to the *Herschel* deblending, which is hard to quantify.

Below a 450 μm flux of 12 mJy, there are 38 non-detections at 500 μm in the figure. This shows SCUBA-2's ability to probe deeper than the *Herschel* data.

Conversely, we can measure the 450 μm counterparts to the 500 μm sources in order to understand the *Herschel* selection. In Figure 4(b), we plot 450 μm flux versus 500 μm flux for all sources in the E11 GOODS-N catalog that lie in the SCUBA-2 area with 450 μm noise < 2.8 mJy. Blends of multiple 450 μm sources at the *Herschel* resolution are seen for some of the brightest sources (red circles). Sources with offsets from the diagonal line may have flux contributions from 450 μm counterparts that are below our flux threshold. The gold circles show sources detected in the *Herschel* 500 μm catalog that are not present in our SCUBA-2 450 μm catalog. For these sources, we measured the 450 μm fluxes directly from the image at the *Herschel* catalog positions. These 450 μm sources may be multiples, where the *Herschel* flux is combining sources that are below our 450 μm flux threshold, and where single-position measurements continue to underestimate the total 450 μm flux. While *Herschel* may be able to pick up such sources, which are not included in our catalog, it is important to stress that one is not learning about individual SMGs from such data.

2.6. Redshifts

We have been compiling spectroscopic redshifts (speczs) from our own Keck observations and from the literature for sources in the GOODS fields for many years, so we have a large database from which to draw from to find redshifts.

In the GOODS-N, many of the speczs were already presented in the SCUBA-2 850 μm and 450 μm tables of Cowie et al. (2017) (i.e., their Tables 5 and 6, respectively). The literature references from which these were drawn include Cohen et al. (2000), Cowie et al. (2004, 2016), Swinbank et al. (2004), Wirth et al. (2004, 2015), Chapman et al. (2005), Treu et al. (2005), Reddy et al. (2006), Barger et al. (2008), Pope et al. (2008), Trouille et al. (2008), Daddi et al. (2009a,b), Cooper et al. (2011), Walter et al. (2012), Bothwell et al. (2013), and Momcheva et al. (2016). There are also three new NOEMA redshifts from Jones et al. (2021).

In the GOODS-S, all of the speczs were already presented in the ALMA redshift table of Cowie et al. (2018) (i.e., their Table 5), apart from one, which we obtained from later Keck/DEIMOS observations. The references for the other redshifts are Szokoly et al. (2004), Casey et al. (2012), Kurk et al. (2013), Inami et al. (2017), and Franco et al. (2018; including B. Mobasher 2018, private communication and G. Brammer 2018, private communication).

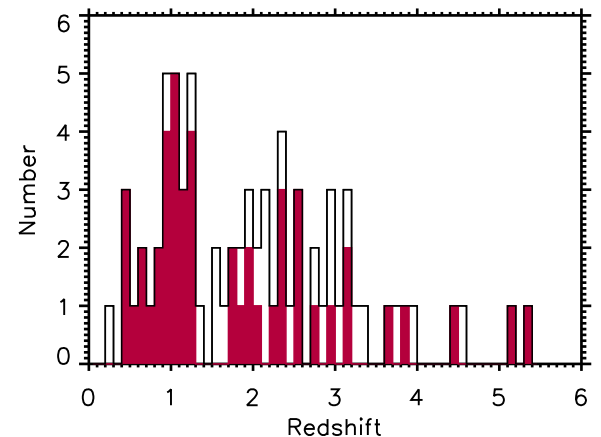


Figure 5. Histogram of the redshift distribution for the 450 μm selected combined GOODS sample. There are 16 sources without either a specz (red shaded histogram) or a photz (open histogram).

In cases where we do not have a specz, we use photometric redshift estimates (photzs) from the literature, though we caution that there is considerable scatter in the estimates from different literature catalogs for optical/NIR faint SMGs (see, e.g., Cowie et al. 2018). For the GOODS-N, we adopt the photzs from the 3D-HST survey of Momcheva et al. (2016), who used a combination of multiband photometry and G141 2D spectral data. We supplement these with photzs from Yang et al. (2014), who used the EAZY code (Brammer et al. 2008) to fit 15 broadbands from the U -band to the infrared (IRAC 4.5 μm) over the Hawaii-Hubble Deep Field North (Capak et al. 2004). For these, we only use the photzs that satisfy their quality flag $Q_z < 1$.

For the GOODS-S, we adopt the photzs from Straatman et al. (2016), who used EAZY to fit the extensive ZFOURGE catalog from 0.3 to 8 μm . None of the photzs in our sample exceed their quality flag $Q < 3$.

We show the redshift distribution for the 450 μm selected combined GOODS sample in Figure 5. After excluding the 16 sources without either a specz or a photz, the median redshift for the remaining 73 sources is $z = 1.99$ with a 68 percent confidence range from 1.55 to 2.10. This is consistent with the median redshifts of $z = 1.95 \pm 0.19$ from Casey et al. (2013) and $z = 1.66 \pm 0.18$ from Zavala et al. (2018). However, as we will discuss in Section 4, median redshifts are not too meaningful when there is such a wide spread in the redshift distribution of the sample.

3. 450 μm NUMBER COUNTS

In order to test the flux calibration and consistency with previous number counts, we construct the differential number counts at 450 μm . Each source contributes $1/(A_e(S)dS)$ to the counts, where A_e is the effective

area where the source can be detected at $> 4\sigma$ given its measured flux density S , and dS is the flux density interval. The error is taken to be Poissonian. We show the raw differential 450 μm number counts for both fields in Figure 6(a), where we compare them with the raw STUDIES counts (Wang et al. 2017; green triangles).

There are observational biases that affect the raw counts. These include flux boosting from Eddington bias (Eddington 1913), spurious sources, source blending, and detection incompleteness. In order to correct the raw counts for these effects to obtain the intrinsic counts, we need to perform Monte Carlo simulations. We do this by first generating source-free maps with only pure noise for each of our fields. These pure noise maps are sometimes referred to as jackknife maps in the literature (see, e.g., Cowie et al. 2002). Following Chen et al. (2013a, 2013b), for each field, we subtract two maps that were each produced by coadding roughly half of the flux-calibrated data. This process subtracts off the real sources, leaving residual maps that are free of any sources. We then rescale the value of each pixel by a factor of $\sqrt{t_1 \times t_2}/(t_1 + t_2)$, with t_1 and t_2 representing the integration time of each pixel from the two maps.

Next, we generate 40 simulated maps for each field by randomly populating our pure noise maps with the same number of sources as in our $> 4\sigma$ samples. We draw these sources from the best-fit broken power law count model of Hsu et al. (2016),

$$\frac{dN}{dS} = \begin{cases} N_0 \left(\frac{S}{S_0} \right)^{-\alpha} & \text{if } S \leq S_0 \\ N_0 \left(\frac{S}{S_0} \right)^{-\beta} & \text{if } S > S_0 \end{cases} \quad (1)$$

where $N_0 = 33.3$, $S_0 = 20.1$, $\alpha = 2.34$, and $\beta = 5.06$.

For each simulated map, we rerun our source extraction down to the 4σ threshold and compute the recovered counts using the same method and flux bins used for the science map. We compare the ratio of the total number of sources from the simulated maps with the input counts. We use all 40 simulations to determine the average ratios as a function of flux, which we then apply to the raw counts to get the corrected counts. We show the corrected number counts for both fields in Figure 6(b), where we compare them with the corrected STUDIES counts (Wang et al. 2017; green triangles).

By using SCUBA-2 observations of cluster fields (A1689, A2390, A370, MACSJ0717.5+3745, MACSJ1149.5+2223, and MACSJ1423.8+2404), Hsu et al. (2016) were able to construct the 450 μm number counts for flux detections ($> 3\sigma$) down to fainter than 1 mJy, thanks to gravitational lensing effects. They used three blank fields (CDF-N, CDF-S, and COSMOS) to cover the brighter fluxes. We show their corrected number counts (black solid circles) and best-fit broken power law (black lines) in both panels of Figure 6. The consistency with Hsu et al. (2016) means it is not necessary

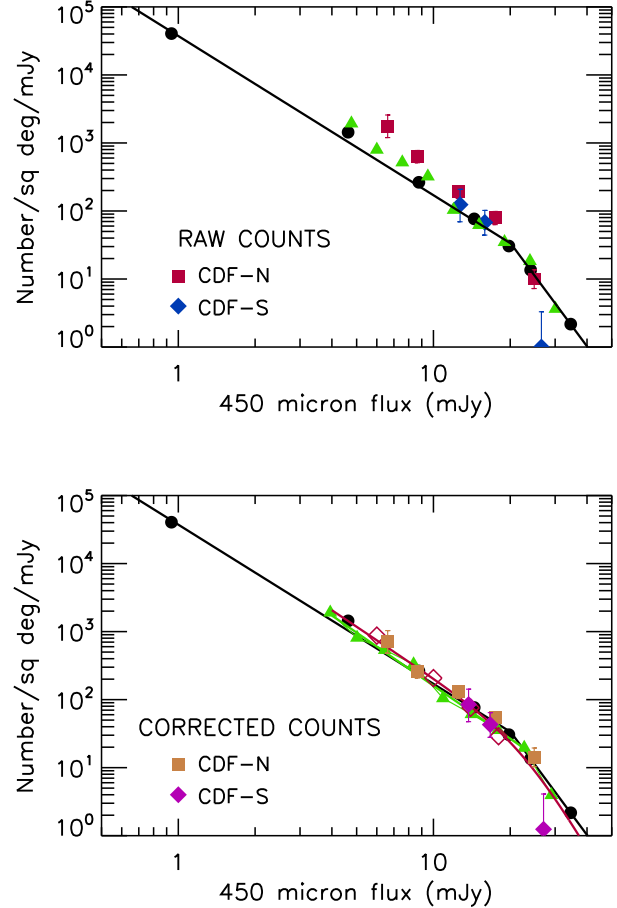


Figure 6. Differential 450 μm (a) raw number counts (red solid squares—CDF-N; blue solid diamonds—CDF-S; green solid triangles—STUDIES from Wang et al. 2017) and (b) corrected number counts (orange solid squares—CDF-N; purple solid diamonds—CDF-S; green solid triangles—STUDIES from Wang et al.; open diamonds—S2CLS EGS from Zavala et al. 2017). In both panels, the Hsu et al. (2016) corrected number counts (black solid circles) and best-fit broken power law (black lines) are shown.

to iterate on the input counts. A multiplicative error of 1.15 in the flux normalization in either direction would result in a significant discrepancy relative to previous counts. We note that the 450 μm counts are very uniform across fields, which is also seen by W.-H. Wang (private communication).

4. FLUX RATIOS

The empirical observation of a tight correlation between thermal dust emission and radio continuum emission (e.g., Helou et al. 1985; Condon et al. 1991), known as the FIR-radio correlation, is thought to result from both quantities being linearly related to the massive SFR (Condon 1992), although we have no good theoreti-

ical understanding of the correlation. If this correlation continues to hold at high redshifts, as evidence suggests it does at least out to $z \sim 5$ (e.g., Barger et al. 2012, 2015; Thomson et al. 2014; Lim et al. 2020), then very sensitive radio observations can be used to localize distant galaxies detected in the submillimeter. In the early days of trying to understand the SCUBA sources, 20 cm data from the VLA were used for just this purpose (e.g., Barger et al. 2000; Smail et al. 2000; Chapman et al. 2003). In combination with the submillimeter data, the 20 cm data have the advantage of allowing crude redshift estimates (sometimes called millimetric redshifts) to be made, based on the opposing spectral slopes of the blackbody spectrum in the submillimeter and the synchrotron spectrum in the radio (e.g., Carilli & Yun 1999; Barger et al. 2000).

FIR/submillimeter flux ratios have also been used to estimate redshifts. For example, Figure 19 of Cowie et al. (2017) showed that for their 850 μm sample in the GOODS-N, $f_{20 \text{ cm}}/f_{850 \mu\text{m}}$ and $f_{250 \mu\text{m}}/f_{850 \mu\text{m}}$ were well correlated, suggesting that both provide a measure of the redshifts. They also found that those with speczs were well segregated by redshift interval. Interestingly, they determined that the scatter in specz versus $f_{20 \text{ cm}}/f_{850 \mu\text{m}}$ was considerably larger than the scatter in specz versus $f_{250 \mu\text{m}}/f_{850 \mu\text{m}}$ (their Figure 20). This is a clear indication that the radio power is not always an accurate measure of the star formation (see Barger et al. 2017 for a detailed analysis of the star-forming galaxies and AGNs in the GOODS-N that lie on the FIR-radio correlation). In contrast, the scatter in specz versus $f_{250 \mu\text{m}}/f_{850 \mu\text{m}}$ is primarily caused by variations in the SEDs of the sources.

Other authors (e.g., Casey et al. 2013; Wang et al. 2019; Lim et al. 2020) have constructed the flux ratios for SMGs in COSMOS and compared them with optical/NIR photzs. Of particular interest is the identification of high-redshift sources. For example, Wang et al. plotted $f_{870 \mu\text{m}}/f_{450 \mu\text{m}}$ versus $z_{\text{phot}} \gtrsim 3$ for their ALMA-detected H -dropouts in their Extended Data Figure 4.

To look for high-redshift candidates in our 450 μm selected combined GOODS sample, in Figure 7(a), we plot $f_{450 \mu\text{m}}/f_{850 \mu\text{m}}$ versus $f_{850 \mu\text{m}}/f_{20 \text{ cm}}$. We color-code the $3 \leq z_{\text{spec}} < 4$ (blue large circles) and $z_{\text{spec}} \geq 4$ sources (red large circles). We adopt the uncertainties on the 450 μm fluxes in the y-axis, since we expect them to be larger than the uncertainties on the 850 μm fluxes, and we adopt the uncertainties on the 850 μm fluxes in the x-axis, since we expect them to be larger than the uncertainties on the 20 cm fluxes. We assign the 20 cm ($> 5\sigma$) flux limits of the two samples to the sources in the radio areas without radio detections (green rightward-pointing arrows).

We can see the good relation between the two flux ratios. A linear fit without considering uncertainties and after excluding source 70, which is located

at the top-left of the plot, gives $\log(f_{450 \mu\text{m}}/f_{850 \mu\text{m}}) = -0.42 \log(f_{850 \mu\text{m}}/f_{20 \text{ cm}}) + 1.40$ (solid line).

We can also see the generally good segregation of the high-redshift sources with speczs from the rest of the population. Thus, we define high-redshift selection criteria based on this plot, namely, $f_{450 \mu\text{m}}/f_{850 \mu\text{m}} < 3$ and $f_{850 \mu\text{m}}/f_{20 \text{ cm}} > 200$ (gold lines). Based on these criteria, we have six candidate high-redshift sources (gold large circles).

In Figures 7(b) and (c), respectively, we show the two axes from (a) separately versus redshift. We again color-code in blue and red the high-redshift sources with speczs. We plot the sources without speczs at a nominal redshift of $z = 0.1$ and without uncertainties, for clarity. In (b), we again show the sources in the radio areas without radio detections as limits (green downward-pointing arrows). In both panels, we show the linear fits as solid lines without considering uncertainties and after excluding source 70, but we only include in the fits those sources having speczs. The resulting fits are (b) $\log(f_{20 \text{ cm}}/f_{850 \mu\text{m}}) = -0.27z - 1.22$ and (c) $\log(f_{450 \mu\text{m}}/f_{850 \mu\text{m}}) = -0.16z + 0.96$.

In each figure, we show the relevant high-redshift criterion from Figure 7(a) as a gold line, and we color in gold the sources that satisfy it. In (b), we have the same high-redshift candidates as in (a), plus one additional candidate. Note that we conservatively consider only a radio limit that is already below the gold line to be a candidate high-redshift source. In (c), we have the same high-redshift candidates as in (a), plus five additional candidates, none of which is the additional candidate found in (b). In both (b) and (c), we plot gold open squares at the redshifts we estimate from the linear fits.

In Table 4, we list the 12 high-redshift candidates that satisfy either the 20 cm/850 μm selection or the 450 $\mu\text{m}/850 \mu\text{m}$ selection that we defined in Figure 7. All of these candidates come from the GOODS-N. We also give their 450 μm , 850 μm , and 20 cm fluxes; their 20 cm/850 μm and 450 $\mu\text{m}/850 \mu\text{m}$ flux ratios; their photzs from Table 2, where available; and the redshifts we estimate from the linear fits in Figures 7(b) and (c), respectively, if the source is a high-redshift candidate based on the figure in question.

Most of the candidates are very faint in the optical/NIR and do not have reliable photzs, but for the five that have photzs, the photzs are consistent with the sources being at high redshift. In combination with three sources with $z_{\text{phot}} \geq 3$ that were not identified as high-redshift candidates in the FIR and seven sources with known $z_{\text{spec}} \geq 3$, we have a total of 22 possible high-redshift sources (we list all of these sources in Table 4).

In Figure 8(a), we show redshift versus 450 μm flux for our 450 μm selected combined GOODS sample, with the high-redshift spectroscopic sources denoted by blue and red circles, the high-redshift candidates selected from

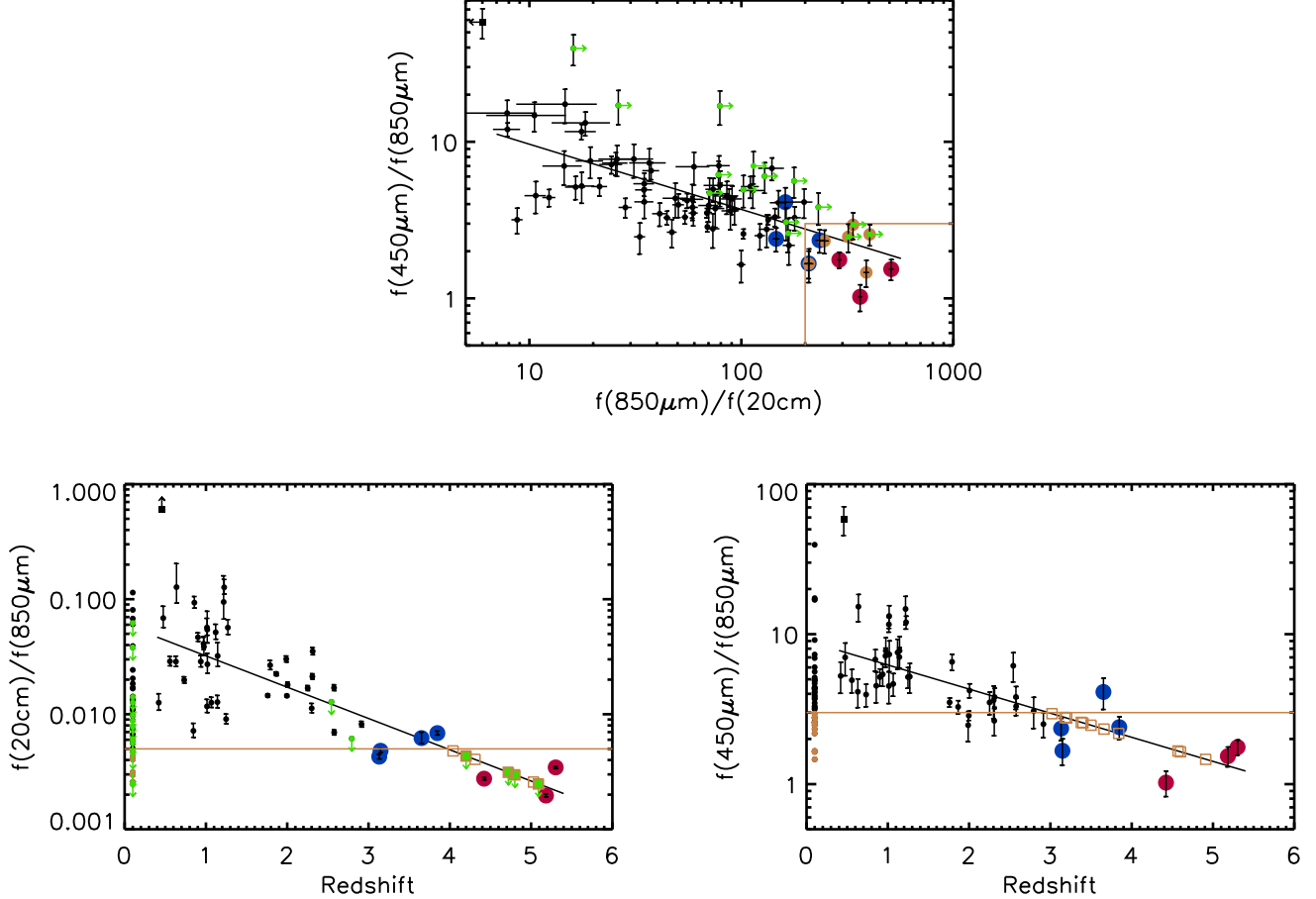


Figure 7. Based on our $450 \mu\text{m}$ selected combined GOODS sample: (a) $450 \mu\text{m}$ to $850 \mu\text{m}$ flux ratio (uncertainties from the $450 \mu\text{m}$ measurements) vs. $850 \mu\text{m}$ to 20 cm flux ratio (uncertainties from the $850 \mu\text{m}$ measurements) for sources with radio data, (b) 20 cm to $850 \mu\text{m}$ flux ratio vs. redshift (uncertainties from the $850 \mu\text{m}$ measurements) for sources with radio data, and (c) $450 \mu\text{m}$ to $850 \mu\text{m}$ flux ratio vs. redshift (uncertainties from the $450 \mu\text{m}$ measurements). Sources with only radio limits are shown in green with (a) rightward-pointing arrows and (b) downward-pointing arrows. In (b) and (c), sources without speczs are placed at a nominal redshift of $z = 0.1$ and shown without uncertainties, for clarity. In all panels, solid lines show simple linear fits to the data, without considering uncertainties and after excluding GOODS-N source 70, which is at the top-left of each plot (black square; arrows denote when its value is off the plot). Sources with $3 \leq z_{\text{spec}} < 4$ are shown in blue, while those with $z_{\text{spec}} \geq 4$ are shown in red. Our adopted high-redshift selection criteria are denoted by gold lines, and the sources that satisfy the (a) combined or (b) and (c) individual criteria but do not have speczs are colored gold. In (b) and (c), we estimate where these sources would lie in redshift based on the given linear fit (gold open squares).

Figure 7 denoted by gold squares (5 of these also have photzs, so in those cases we use the photzs; we use $z_{450/850}$ for 6 sources; and for the last source, which was not identified as a high-redshift candidate from the $450 \mu\text{m}/850 \mu\text{m}$ flux ratio, we use $z_{20/850}$), and the three additional high-redshift photz sources denoted by blue diamonds. The redshift distribution at every flux is very large, demonstrating why quoting a median redshift for the sample as a whole is not particularly meaningful.

High-redshift sources can also be picked out by their faintness in the MIR. In Figure 8(b), we plot redshift versus $4.5 \mu\text{m}$ flux for the $450 \mu\text{m}$ selected sample ly-

ing within the *HST*/ACS footprint of the GOODS-N. We used the Barro et al. (2019) catalog for the $4.5 \mu\text{m}$ fluxes. For the small number of sources not in the catalog, we measured the $4.5 \mu\text{m}$ fluxes on the *Spitzer*/IRAC image using a $3''$ diameter aperture and obtained the normalization by matching to sources in the catalog.

For the sources with a measured $4.5 \mu\text{m}$ flux and either a specz, a photz, or a FIR redshift from Table 4, there is a strong correlation of redshift with $4.5 \mu\text{m}$ flux, with all of the $z \geq 3$ sources having fluxes below 0.014 mJy. This alternate high-redshift diagnostic provides a strong con-

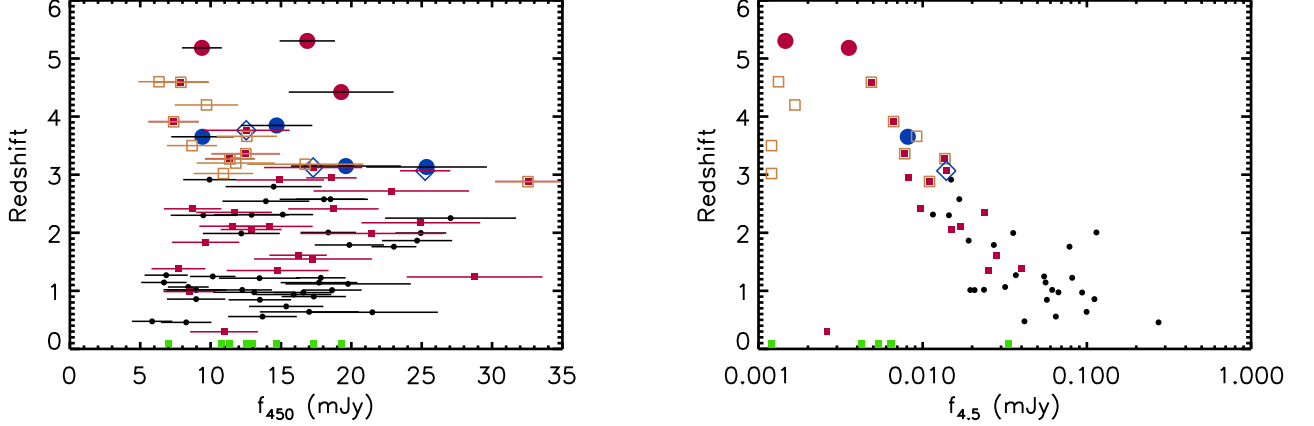


Figure 8. (a) Redshift vs. $450 \mu\text{m}$ flux (with uncertainties) for the $450 \mu\text{m}$ selected combined GOODS sample. (b) Redshift vs. $4.5 \mu\text{m}$ flux for the sources in the $450 \mu\text{m}$ selected GOODS-N sample that lie within the *HST*/ACS footprint. We use the Barro et al. (2019) catalog for most of the $4.5 \mu\text{m}$ fluxes, but for the small number of sources not in that catalog, we measured the fluxes ourselves. Note that the uncertainties on the $4.5 \mu\text{m}$ fluxes are smaller than the data points. In both panels, sources with $\text{specz} < 3$ are shown as black circles, while sources with photz are shown as red squares. Sources with $3 \leq z_{\text{spec}} < 4$ are denoted by blue large circles, while those with $z_{\text{spec}} \geq 4$ are denoted by red large circles. The high-redshift candidates from Table 4 are denoted by gold open squares (we use the photz for the five that have a photz). Sources with $3 \leq z_{\text{phot}} < 4$ that were not also identified as high-redshift candidates from the FIR are enclosed in blue large open diamonds. Finally, sources without either a specz or a photz and not identified as high-redshift candidates from the FIR are placed at a nominal redshift of $z = 0.1$ and shown as green squares without uncertainties, for clarity.

firmation of the high-redshift candidate selection from the FIR.

It is clear that using FIR methods to identify high-redshift candidates that cannot be found with photz is critical, or else the redshift distribution for $450 \mu\text{m}$ selected samples will not be complete and will be biased to lower redshifts.

5. SED FITTING

We next want to determine the SFRs and dust temperatures of the $450 \mu\text{m}$ selected samples. We obtain best fits to the SMGs' full SEDs using the publicly available Bayesian energy-balance SED-fitting code MAGPHYS (da Cunha et al. 2015). We fit at the adopted redshifts (see Section 2.6), and we do not allow the redshift to vary to optimize the SED fit. The SED fits give SFRs (from the total bolometric luminosities; these are 100 Myr averages for a Chabrier 2003 initial mass function, or IMF) and dust properties, together with their error ranges. We note that SFRs are relatively insensitive to redshift for dust-dominated galaxies.

For illustrative purposes, in Figure 9, we show the SEDs (colored symbols) and the MAGPHYS fits (black curve) for each $450 \mu\text{m}$ source in the GOODS-S sample (i.e., Table 3) that lies in the CANDELS region, alongside two multiwavelength thumbnails (FIR/submillimeter on top and optical/NIR on bottom). The SED plots are labeled at the top with the specz or photz , the χ^2 value for the fit, and the SFR. Note that there is no SED plot for source 4, since the

ALMA position for that source is on the edge of another source, and thus the photometry is contaminated.

The MAGPHYS infrared SEDs contain multiple temperature components, which provide an average, luminosity-weighted dust temperature (see da Cunha et al. 2015's Equation 8). We shall generally adopt these temperatures. However, we note that at low redshifts, where the short wavelength FIR data are relatively unconstraining, MAGPHYS may insert hot components that raise the temperatures and FIR luminosities. In order to check the reality of these components, we also constructed gray body fits for our $450 \mu\text{m}$ selected GOODS-N sample using an optically thin, single temperature modified blackbody, $S_\nu \propto \nu^\beta B_\nu(T)$ (e.g., see Klaas et al. 1997). Both the MAGPHYS and the gray body fits assume $\beta = 1.5$.

Fourteen of the sources have observed-frame $70 \mu\text{m}$ fluxes, and these fluxes were not used in either the MAGPHYS or the gray body fits. In Figure 10, we show example comparisons of the two fits (MAGPHYS in red and gray body in green), along with an Arp 220 SED (black). For the two higher-redshift sources shown (top row; sources 20 and 31), the MAGPHYS and gray body fits are similar and return nearly identical dust temperatures. Source 20 has a $70 \mu\text{m}$ measurement (gold square) consistent with the fitted SED; source 31 does not have a $70 \mu\text{m}$ measurement. However, for the two lower-redshift sources (bottom row; sources 25 and 39), MAGPHYS includes a hot component that substan-

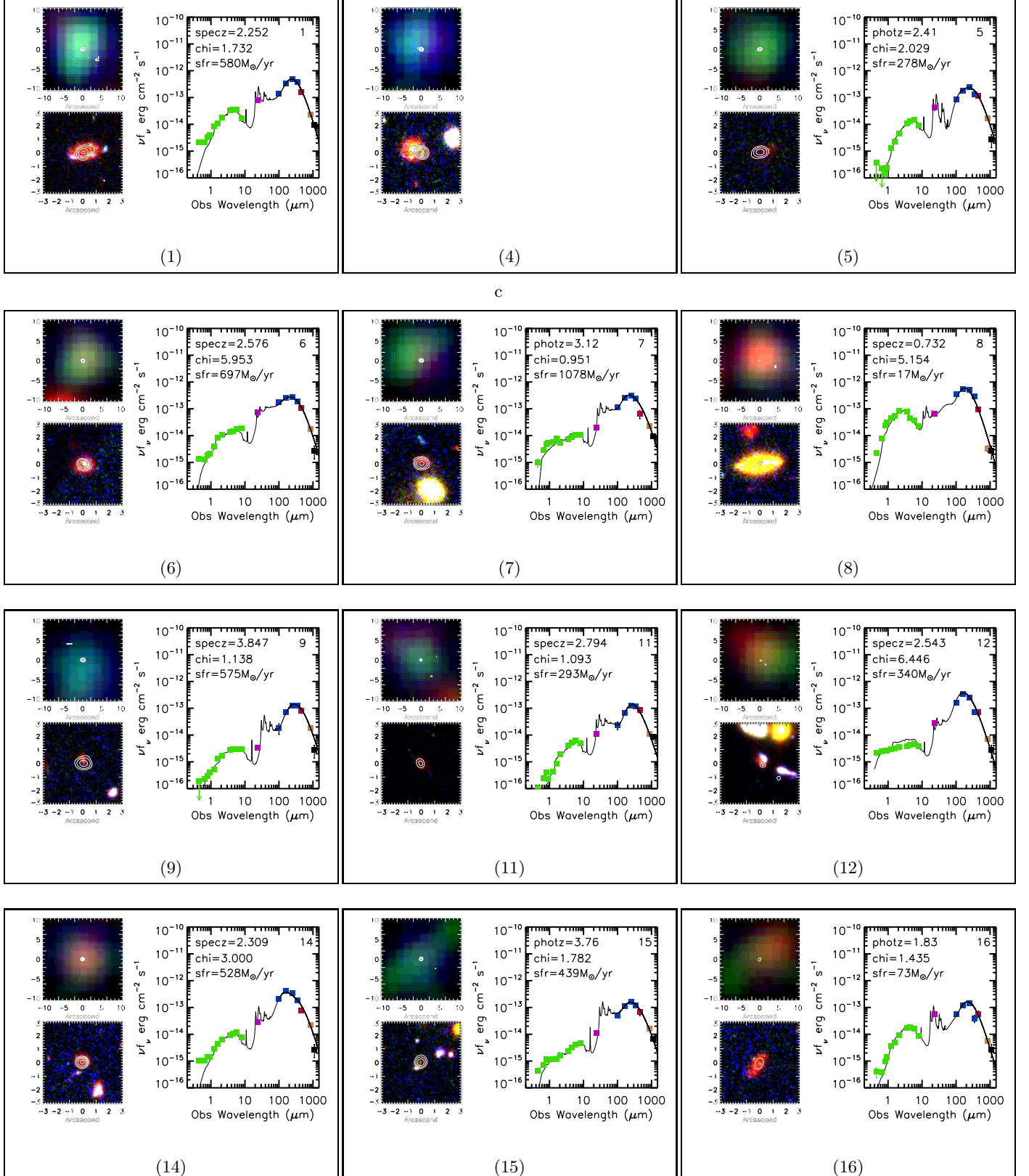


Figure 9. All 450 μm selected sources in the GOODS-S (i.e., Table 3; source numbers on bottom) that lie in the CANDELS region. (Right in each panel): Multiwavelength SEDs (green—*HST* and *Spitzer*/IRAC optical/NIR; pink—*Spitzer*/MIPS 24 μm ; blue—*Herschel* FIR; red—SCUBA-2 450 μm ; gold—ALMA 870 μm ; black—ALMA 1.1 mm) and MAGPHYS fit (black curve). The SED plots are labeled at the top-right with the source number and at the top-left with the specz or the photz, the χ^2 value for the fit, and the SFR. (Left in each panel): two thumbnail images showing (top) a combination of *Herschel*/PACS 100 μm (blue), SCUBA-2 450 μm (green), and SCUBA-2 850 μm (red) data, and (bottom) a combination of *HST* F435W (blue), F814W (green), and F160W (red) data. The contours are ALMA 870 μm . Note that the ALMA position for source 4 is on the edge of another source (see bottom-left thumbnail), so no SED was constructed due to contamination of the photometry.

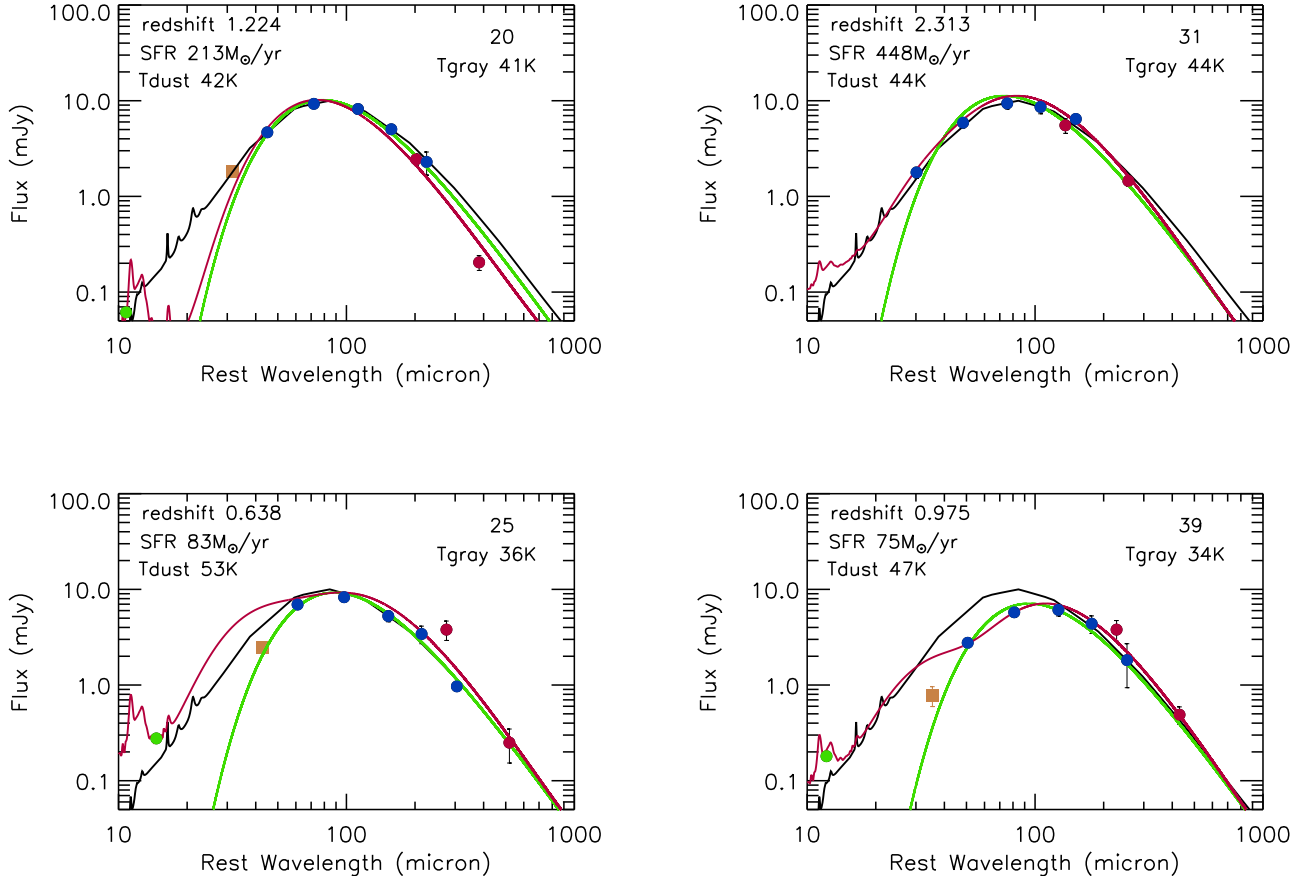


Figure 10. SEDs for four example sources from the 450 μm selected GOODS-N sample. Where available, we show the 70 μm flux with gold squares. The curves are Arp 220 (black), MAGPHYS fits (red), and gray body fits (green). (Top row) Two higher-redshift examples where the MAGPHYS and gray body fits are consistent and also similar to Arp 220. (Bottom row) Two lower-redshift examples where the MAGPHYS fit includes a hot component that is inconsistent with the 70 μm flux.

tially raises the temperature above the gray body fit. Both of these sources have 70 μm measurements that are strongly inconsistent with the MAGPHYS SED but agree roughly with the gray body fits.

We conclude that the gray body fits are preferred at lower redshifts, noting that this also reduces the FIR luminosities and SFRs for these sources. In our subsequent analyses, we will adopt the SFRs and dust temperatures derived from the gray body fits when we extend to sources below $z = 1$.

6. MAGPHYS STAR FORMATION RATES AND FIR LUMINOSITIES

In this section, we examine the SFRs and FIR luminosities that MAGPHYS outputs for the 450 μm selected combined GOODS sample sources with $z > 1$.

In Figure 11(a), we plot $L_{8-1000 \mu\text{m}}$ versus SFR. A simple linear fit gives

$$\log \text{SFR} (M_\odot \text{ yr}^{-1}) = \log L_{8-1000 \mu\text{m}} (\text{erg s}^{-1}) - 43.71, \quad (2)$$

which we denote on the figure by a solid line. For comparison, Murphy et al. (2011) determined a theoretical conversion of -43.41 between the two terms, which they computed from a Starburst99 (Leitherer et al. 1999) constant SFR model and a Kroupa (2001) IMF. For a Chabrier IMF, this would correspond to -43.38 . We denote this relation by the dashed line. Meanwhile, Madau & Dickinson (2014) adopted -43.52 using Kennicutt (1998), after conversion to a Chabrier IMF from their Salpeter (1955) IMF. We denote this relation by the dotted line. Both of these relations give slightly lower SFRs than the MAGPHYS relation. This emphasizes the uncertainty in the $L_{8-1000 \mu\text{m}}$ to SFR calibration.

In Figure 11(b), we verify empirical expectations for a correlation between $L_{8-1000 \mu\text{m}}$ and radio power. We determine the latter independently of MAGPHYS using

$$P_{20 \text{ cm}} = 4\pi d_L^2 f_{20 \text{ cm}} 10^{-29} (1+z)^{\alpha-1} \text{ erg s}^{-1} \text{ Hz}^{-1}. \quad (3)$$

Here d_L is the luminosity distance (cm) and $f_{20 \text{ cm}}$ is the 20 cm flux in units of μJy . This equation assumes that the radio flux density goes as $\nu^{-\alpha}$. Following Barger et al. (2017), we adopt a radio spectral index of $\alpha = 0.8$ (Condon 1992; Ibar et al. 2010; An et al. 2021). The solid line shows the median FIR-radio correlation for star-forming galaxies from Barger et al., and the dotted lines show a multiplicative factor of 3 of this value, which Barger et al. considered to be the region where sources lie on the FIR-radio correlation. The current data are well-represented by the Barger et al. correlation.

In Figure 11(c), we plot SFR versus SCUBA-2 850 μm flux. A simple linear fit to the data, not considering uncertainties on the data, gives

$$\log \text{SFR} = 1.12 \log f_{850 \mu\text{m}} + 1.70, \quad (4)$$

which we denote on the figure by a solid line. There may be a shift to higher SFRs for brighter sources in

our sample. The slope in our relation is steeper than that in Dudzevičiūtė et al. (2020), who found

$$\log \text{SFR} = 0.42 \log f_{870 \mu\text{m}} + 2.19 \quad (5)$$

for 517 AS2UDS¹ sources with redshifts between $z = 1.8$ and $z = 3.4$. We denote their relation on the figure as a dashed line. The reason for the disagreement is not clear.

In Figure 11(d), we plot SFR versus redshift. The present results are broadly consistent with the maximum SFR from Barger et al. (2017), namely $1000 M_\odot \text{ yr}^{-1}$ (dashed line), above which there are relatively few galaxies (see also Karim et al. 2013 and Barger et al. 2014). The Barger et al. (2017) value is based on the Murphy et al. (2011) relation and a Kroupa IMF, and the primary uncertainty is the calibration of the SFR.

7. DISCUSSION

Most comparisons of 450 μm and 850 μm selected samples have argued that the 450 μm samples peak at lower redshifts (e.g., Casey et al. 2013; Zavala et al. 2018; Lim et al. 2020) and may be biased to higher dust temperatures (Casey et al. 2013; Lim et al. 2020). Such sample differences are clearly introduced by the SED shape, where $f_{450 \mu\text{m}}/f_{850 \mu\text{m}}$ becomes smaller as one moves to higher redshifts (see Figure 7(c)) and larger as one moves to higher dust temperatures. However, as Lim et al. (2020) emphasize, these selection biases are very dependent on the relative depths of the 450 μm and 850 μm samples, since the dust temperature is strongly dependent on the FIR luminosity, and submillimeter samples are biased to higher FIR luminosities at higher redshifts.

7.1. Are the Redshift Distributions Different for a 450 μm versus an 850 μm Selection?

In Figure 12(a), we show the 850 μm fluxes from Tables 2 and 3 measured for the 450 μm selected combined GOODS sample versus redshift. The horizontal line shows the SCUBA-2 1.65 mJy (4σ) confusion limit at 850 μm . As was also noted by Zavala et al. (2018), all of the sources above $z = 1.5$ (vertical line) would be included in an 850 μm sample, and the 450 μm selection only adds sources that would not be found in an 850 μm sample below $z = 1.5$.

In Figure 12(b) (bottom histogram), we show the redshift distribution of the 450 μm selected combined GOODS sample (black line histogram). The red shading shows the sources in this sample that are detected above 1.65 mJy at 850 μm . In Figure 12(b) (top histogram), we show the redshift distribution of the 58 sources with

¹ AS2UDS (Stach et al. 2019) is an ALMA 870 μm follow-up survey of 716 $> 4\sigma$ SCUBA-2 sources (corresponding to observed 850 μm fluxes ≥ 3.4 mJy) detected in the SCUBA-2 Cosmology Legacy Survey (S2CLS; Geach et al. 2017) 850 μm map of the UKIDSS Ultra Deep Survey field.

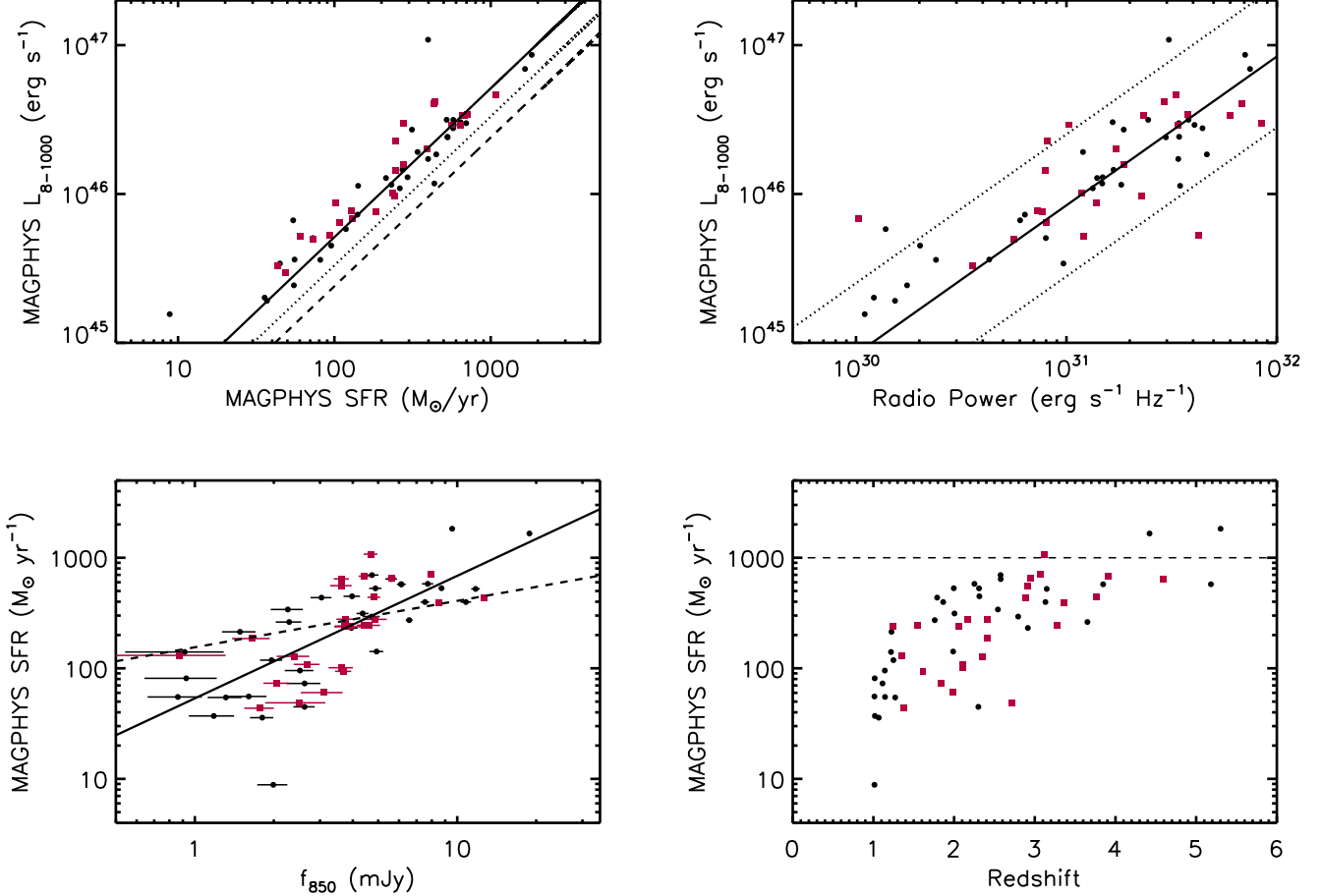


Figure 11. Based on the 450 μm selected combined GOODS sample with either $z_{\text{spec}} > 1$ or a $z_{\text{phot}} > 1$: (a) MAGPHYS FIR luminosity vs. MAGPHYS SFR, (b) MAGPHYS FIR luminosity vs. radio power, (c) MAGPHYS SFR vs. SCUBA-2 850 μm flux (with uncertainties on the flux), and (d) MAGPHYS SFR vs. redshift. Sources with speczs are shown as black circles, while sources with photzs are shown as red squares. In (a), the solid line shows a simple linear fit to the two MAGPHYS outputs, while the dashed line shows the relation (after conversion to a Chabrier IMF) from Murphy et al. (2011; their Equation 4), and the dotted line shows the relation (after conversion to a Chabrier IMF) adopted by Madau & Dickinson (2014), which is based on Kennicutt (1998). In (b), the solid line shows the median FIR-radio correlation for star-forming galaxies from Barger et al. (2017) (calculated from their Equation 3, using a parameterization of 2.35, and their Equation 4), and the dotted lines show a multiplicative factor of 3 of this value, which they considered to be the region where sources lie on the FIR-radio correlation. In (c), the solid line shows shows a simple linear fit to the data (this paper’s Equation 4), and the dashed line shows, for comparison, the linear relation from Dudzevičiūtė et al. (2020) (given in this paper’s Equation 5). In (d), the dashed line shows the maximum SFR for galaxies from Barger et al. (2017) based on the Murphy et al. (2011) relation and a Kroupa IMF, which is very similar to a Chabrier IMF (see text in Section 6).

fluxes > 1.65 mJy in the GOODS-S ALMA 870 μm sample of Cowie et al. (2018) (blue histogram). A Mann-Whitney test shows no statistically significant difference between the blue histogram and the red histogram.

Restricting the 450 μm selected sample to sources that would be present in the SCUBA-2 confusion-limited (> 1.65 mJy) 850 μm selected sample raises the median redshift to $z = 2.30$ from the $z = 1.99$ value noted previously for the full 450 μm sample. However, as we have emphasized, there is a wide distribution of red-

shifts, and the median is a poor characterization of this distribution.

This situation is best summarized by noting that the two distributions are quite similar for the higher redshift sources, but the 450 μm sample adds in lower redshift sources, which results in the reduction of the median.

7.2. Do Dust Temperatures Evolve with Redshift?

Many previous papers have noted strong evolution in dust temperature with both redshift and FIR luminos-

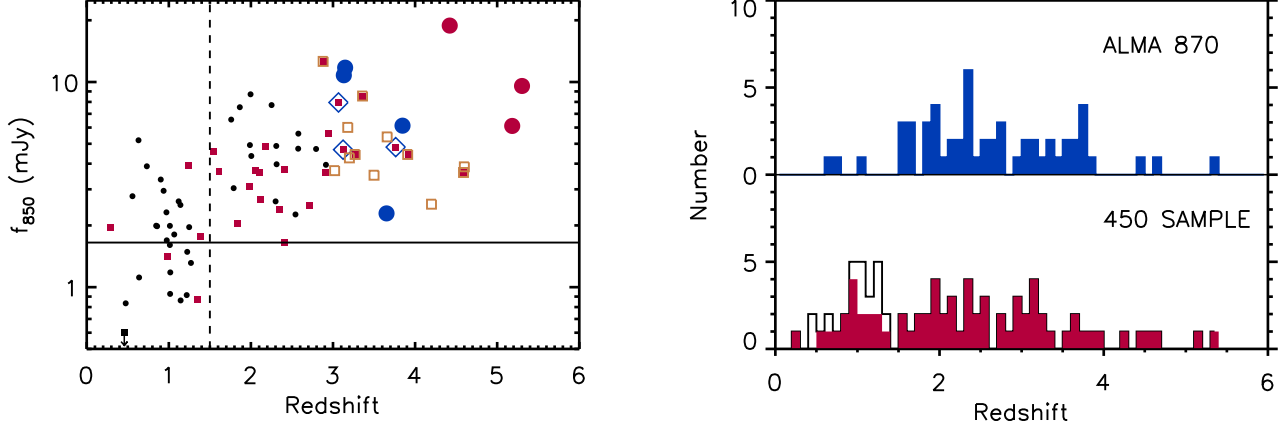


Figure 12. (a) SCUBA-2 850 μm flux vs. redshift for the 450 μm selected combined GOODS sample. Sources with $z_{spec} < 3$ are shown as black circles, while sources with z_{phot} are shown as red squares. Sources with $3 \leq z_{spec} < 4$ are denoted by blue large circles, while those with $z_{spec} \geq 4$ are denoted by red large circles. The high-redshift candidates from Table 4 are denoted by gold open squares (we use the photzs for the five that have a photz). Sources with $3 \leq z_{phot} < 4$ that were not also identified as high-redshift candidates from the FIR are enclosed in blue large open diamonds. GOODS-N source 70 (bottom-left of the plot) is denoted by a black square with a downward pointing arrow, indicating it is off the plot. The horizontal line shows the SCUBA-2 1.65 mJy (4σ) confusion limit at 850 μm , and the dashed vertical line shows the redshift $z = 1.5$ above which all of the 450 μm sources would be found in an 850 μm sample. (b) Redshift distributions for the 450 μm selected combined GOODS sample (bottom histogram; shaded region shows the sample that has SCUBA-2 850 μm fluxes $> 1.65 \mu\text{Jy}$) and for the $> 1.65 \mu\text{Jy}$ ALMA 870 μm GOODSS sample of Cowie et al. (2018) (top histogram). We do not show the eight 450 μm sources without any redshift information in either (a) or (b).

ity (e.g., Magnelli et al. 2013; Swinbank et al. 2014; Béthermin et al. 2015; Schreiber et al. 2018; Zavala et al. 2018). If the effective area over which the galaxy radiated were constant as a function of both redshift and FIR luminosity, then there would be a simple monotonic relation between FIR luminosity and dust temperature. However, when we measure the evolution of FIR luminosity, we are also measuring the evolution in the galaxy properties. There is a dependence of FIR luminosity on dust temperature, but it is not the sole dependence.

We show the evolution in dust temperature for the present 450 μm selected GOODS-N sample in Figures 13(a) and 13(b), respectively. In both panels, we code the data points by redshift. From Figure 13(a), we see that there is a strong increase in dust temperature with redshift. From Figure 13(b), we see that there is a strong increase in dust temperature with FIR luminosity.

However, there is controversy over whether the evolution of the dust temperature with redshift is a real effect or simply a consequence of the selection bias to higher FIR luminosity as we move to higher redshifts. Most recently, Lim et al. (2020) and Dudzevičiūtė et al. (2020) did not find any evidence for redshift evolution in a uniform FIR luminosity subsample of their data. Using a spectroscopically complete 1.4 mm selected South Pole Telescope high-redshift, strongly gravitationally lensed

sample, Reuter et al. (2020) also found that their data could be consistent with no evolution.

Our data agree with these recent results. From Figure 13(b), we can see at once that at the high FIR luminosity end for this relatively small sample, the range of dust temperatures is similar for both high ($z > 3$) and more moderate ($z < 3$) redshift sources. We look at this in more detail in Figure 14. Here we restrict to sources with redshifts $z < 3$ and $L_{8-1000 \mu\text{m}} > 2 \times 10^{12} L_{\odot}$, where we expect our sample to be substantially complete. We find no statistically significant evidence of evolution with redshift with a Pearson coefficient of $R = 0.3433$.

7.3. Do 450 μm Samples Select Warmer Sources Than an 850 μm Sample?

As we discussed in Section 7.1, the 450 μm selection only adds sources that would not be found in an 850 μm sample below $z = 1.5$. We characterize the evolution in $f_{450 \mu\text{m}}/f_{850 \mu\text{m}}$ with redshift by using the fitted MAGPHYS SEDs for the 450 μm selected GOODS-N sample sources and determining what the $f_{450 \mu\text{m}}/f_{850 \mu\text{m}}$ values would be if the lower-redshift sources were moved up in redshift. In Figure 15, we show predicted $f_{450 \mu\text{m}}/f_{850 \mu\text{m}}$ versus redshift (black curves) for all of the sources with $z < 1.5$. We compare these with the measured values for all the sources with $z > 1.5$ (squares; color-coded by the MAGPHYS dust temperature: blue $< 40 \text{ K}$; green=40–50 K; red $> 50 \text{ K}$).

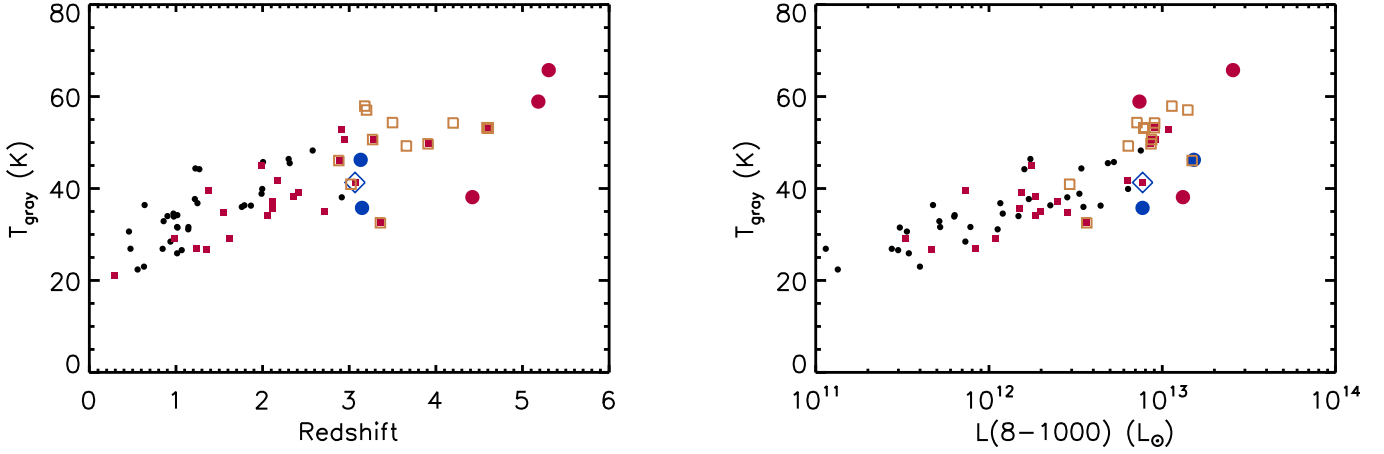


Figure 13. Gray body dust temperature vs. (a) redshift and (b) $L_{8-1000 \mu\text{m}}$ for our $450 \mu\text{m}$ selected GOODS-N sample with gray body temperature measurements. Sources with $z_{\text{spec}} < 3$ are shown as black small circles. Sources with z_{phot} are shown as red small squares. Sources with $3 \leq z_{\text{spec}} < 4$ are denoted by blue large circles, while those with $z_{\text{spec}} \geq 4$ are denoted by red large circles. The high-redshift candidates from Table 4 are denoted by gold open squares (we use the photzs for the five that have a photz). A source with $3 \leq z_{\text{phot}} < 4$ that was not also identified as a high-redshift candidate from the FIR is enclosed in a blue large open diamond.

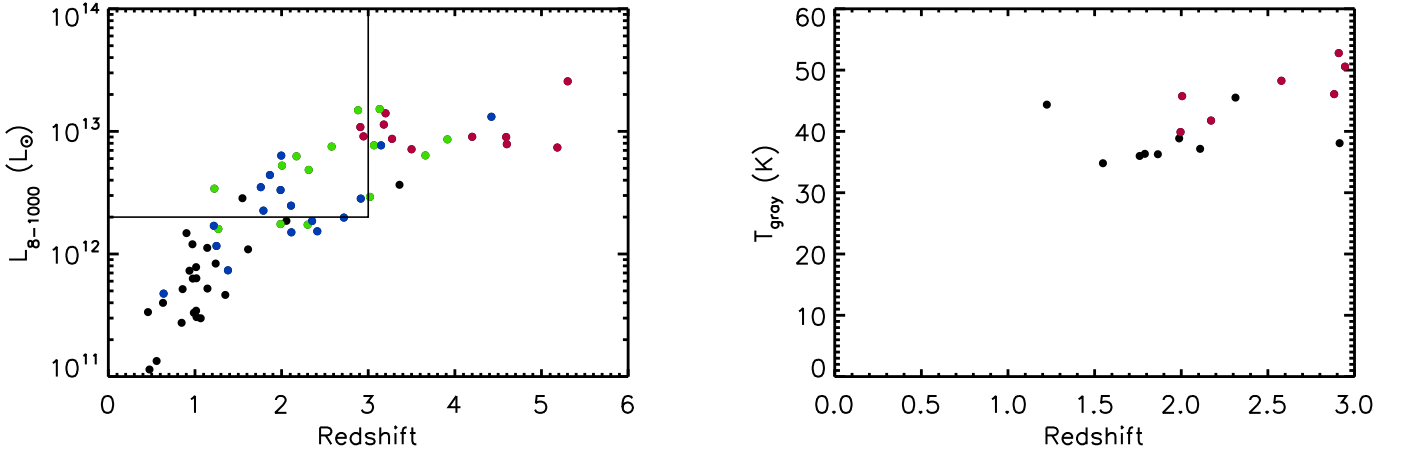


Figure 14. (a) $L_{8-1000 \mu\text{m}}$ and (b) gray body dust temperature (from selected region in (a)) vs. redshift for our $450 \mu\text{m}$ selected GOODS-N sample with gray body temperature measurements. In (a), the symbols are color-coded by temperature (black < 35 K; blue = 35–40 K; green = 40–50 K; red > 50 K). The temperatures are strongly correlated with $L_{8-1000 \mu\text{m}}$. The black lines show a restricted region with redshifts $z < 3$ and $L_{8-1000 \mu\text{m}} > 2 \times 10^{12} L_{\odot}$ where our sample should be substantially complete. In (b), we show sources from only that restricted region. The symbols are color-coded by $L_{8-1000 \mu\text{m}}$ (black > $2 \times 10^{12} L_{\odot}$; red > $5 \times 10^{12} L_{\odot}$).

The higher-redshift sources are consistent with having the same SEDs as the lower-redshift sources (i.e., the squares lie in the range of the extrapolated lower-redshift values). Thus, there is no evidence for the selection of warmer sources with a 450 μm sample than with an 850 μm sample.

8. SUMMARY

In this fifth paper in our SUPER GOODS series, we presented SCUBA-2 450 μm selected samples in the two GOODS fields. Our main results are as follows:

- We constructed the differential number counts at 450 μm and found excellent agreement with results in the literature.
- We used the extensive redshift information available on the GOODS fields to see how well redshifts could be estimated from simple flux ratios (20 cm/850 μm and 450 μm /850 μm). We found tight correlations for both ratios with redshift.
- We provided a table of 12 high-redshift candidates based on these correlations. Most of the candidates are very faint in the optical/NIR and do not have reliable photzs, but for the five that have photzs, the photzs are consistent with the sources being at high redshift.
- We found a strong correlation of redshift with 4.5 μm flux. This alternate high-redshift diagnostic strongly confirms our high-redshift candidate selection. Without FIR methods to identify high-redshift candidates that cannot be found with photzs, the redshift distribution for 450 μm selected samples is not complete and is biased to lower redshifts.
- We found a wide distribution of redshifts for the 450 μm selected sample, making the median redshift a poor characterization of this distribution.
- We constructed full SEDs and used the publicly available SED-fitting code MAGPHYS (da Cunha et al. 2015) to obtain best fits at our adopted redshifts. These SED fits gave SFRs and dust properties for our 450 μm selected samples.
- At low redshifts, MAGPHYS may insert hot components that raise the temperatures and FIR luminosities of the sources. We checked these components by also constructing gray body fits for our 450 μm selected GOODS-N sample. Through comparisons with observed-frame 70 μm fluxes that were not included in either type of fit, we concluded that the gray body fits are preferred at $z < 1$.
- We found that the 450 μm selected sample introduces a number of $z < 1.5$ sources, but beyond this, there is no difference in the redshift distributions for 450 μm and 850 μm samples.
- We find that the observed evolution of dust temperature with redshift is primarily driven by a selection bias of higher FIR luminosities at higher redshifts.
- We did not find evidence that warmer sources are selected in a 450 μm sample than in an 850 μm sample.

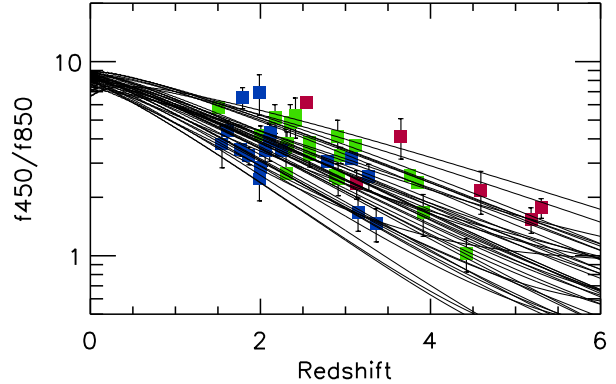


Figure 15. Predicted $f_{450 \mu\text{m}}/f_{850 \mu\text{m}}$ vs. redshift (black curves) for all of the 450 μm selected sources in the GOODS-N with $z < 1.5$ based on the fitted MAGPHYS SEDs. Squares show the measured values for all the sources with $z > 1.5$, color-coded by the MAGPHYS dust temperature (blue $< 40 \text{ K}$; green=40–50 K; red $> 50 \text{ K}$).

ACKNOWLEDGMENTS

We thank the anonymous referee for a very constructive report that helped us to improve the manuscript. We gratefully acknowledge support for this research from the William F. Vilas Estate and a Kellett Mid-Career Award and a WARF Named Professorship from the University of Wisconsin-Madison Office of the Vice Chancellor for Research and Graduate Education with funding from the Wisconsin Alumni Research Foundation (A.J.B.), NASA grants NNX17AF45G and 80NSSC22K0483 (L.L.C.), a Wisconsin Space Grant Consortium (WSGC) Undergraduate Scholarship (A.H.B.), and a WSGC Graduate and Professional Research Fellowship (L.H.J.).

The James Clerk Maxwell Telescope is operated by the East Asian Observatory on behalf of The National Astronomical Observatory of Japan, Academia Sinica Institute of Astronomy and Astrophysics, the Korea Astronomy and Space Science Institute, the National Astronomical Observatories of China and the Chinese Academy of Sciences (grant No. XDB09000000), with additional funding support from the Science and Technology Facilities Council of the United Kingdom and participating universities in the United Kingdom and Canada. The W. M. Keck Observatory is operated as a scientific partnership among the California Institute of Technology, the University of California, and NASA, and was made possible by the generous financial support of the W. M. Keck Foundation. The authors wish to recognize and acknowledge the very significant cultural role and reverence that the summit of Maunakea

has always had within the indigenous Hawaiian commu-

nity. We are most fortunate to have the opportunity to conduct observations from this mountain.

REFERENCES

- An, F., Vaccari, M., Smail, I., et al. 2021, MNRAS, 507, 2643
- Ashby, M. L. N., Willner, S. P., Fazio, G. G., et al. 2015, ApJS, 218, 33
- Balestra, I., Mainieri, V., Popesso, P., et al. 2010, A&A, 512, 12
- Barger, A. J., Cowie, L. L., Bauer, F. E., et al. 2019, ApJ, 887, 23
- Barger, A. J., Cowie, L. L., Chen, C.-C., et al. 2014, ApJ, 784, 9
- Barger, A. J., Cowie, L. L., Owen, F. N., et al. 2015, ApJ, 801, 87
- Barger, A. J., Cowie, L. L., Owen, F. N., Hsu, L.-Y., & Wang, W.-H. 2017, ApJ, 835, 95
- Barger, A. J., Cowie, L. L., & Richards, E. A. 2000, AJ, 119, 2092
- Barger, A. J., Cowie, L. L., Sanders, D. B., et al. 1998, Nature, 394, 248
- Barger, A. J., Cowie, L. L., & Wang, W.-H. 2008, ApJ, 689, 687
- Barger, A. J., Wang, W.-H., Cowie, L. L., et al. 2012, ApJ, 761, 89
- Barro, G., Pérez-González, P. B., Cava, A., et al. 2019, ApJS, 243, 22
- Béthermin, M., Daddi, E., Magdis, G., et al. 2015, A&A, 573, 113
- Bothwell, M. S., Smail, I., Chapman, S. C., et al. 2013, MNRAS, 429, 3047
- Brammer, G. B., van Dokkum, P. G., & Coppi, P. 2008, ApJ, 686, 1503
- Capak, P., Cowie, L. L., Hu, E. M., et al. 2004, AJ, 127, 180
- Carilli, C. L., & Yun, M. S. 1999, ApJ, 513, L13
- Casey, C. M., Chen, C.-C., Cowie, L. L., et al. 2013, MNRAS, 436, 1919
- Chabrier, G. 2003, PASP, 115, 763
- Chapman, S. C., Barger, A. J., Cowie, L. L., et al. 2003, 585, 57
- Chapman, S. C., Blain, A. W., Smail, I., & Ivison, R. J. 2005, ApJ, 622, 772
- Chen, C.-C., Cowie, L. L., Barger, A. J., et al. 2013a, ApJ, 762, 81
- Chen, C.-C., Cowie, L. L., Barger, A. J., et al. 2013b, ApJ, 776, 131
- Condon, J. J. 1992, ARA&A, 30, 575
- Condon, J. J., Anderson, M. L., & Helou, G. 1991, ApJ, 376, 95
- Cooper, M. C., Aird, J. A., Coil, A. L., et al. 2011, ApJS, 193, 14
- Cowie, L. L., Barger, A. J., Hsu, L.-Y., et al. 2017, ApJ, 837, 139
- Cowie, L. L., Barger, A. J., Hu, E. M., Capak, P., & Songaila, A. 2004, AJ, 127, 3137
- Cowie, L. L., Barger, A. J., & Songaila, A. 2016, ApJ, 817, 57
- Cowie, L. L., González-López, J., Barger, A. J., et al. 2017, ApJ, 837, 139
- da Cunha, E., Walter, F., Smail, I. R., et al. 2015, ApJ, 806, 110
- Daddi, E., Dannerbauer, H., Krips, M., et al. 2009a, ApJL, 695, L176
- Daddi, E., Dannerbauer, H., Stern, D., et al. 2009b, ApJ, 694, 1517
- Dudzevičiūtė, U., Smail, I., Swinbank, A. M., et al. 2020, MNRAS, 494, 3828
- Eales, S., Lilly, S., Gear, W., et al. 1999, ApJ, 515, 518
- Eddington, A. S. 1913, MNRAS, 73, 359
- Elbaz, D., Dickinson, M., Hwang, H. S., et al. 2011, A&A, 533, A119 (E11)
- Franco, M., Elbaz, D., Béthermin, M., et al. 2018, A&A, 620, A152
- Geach, J. E., Chapin, E. L., Coppin, K. E. K., et al. 2013, MNRAS, 432, 53
- Geach, J. E., Dunlop, J. S., Halpern, M., et al. 2017, MNRAS, 465, 1789
- Giavalisco, M., Dickinson, M., Ferguson, H. C., et al. 2004, ApJ, 600, L93
- Grogan, N. A., Kocevski, D. D., Faber, S. M., et al. 2011, ApJS, 197, 35
- Guo, Y., Ferguson, H. C., Giavalisco, M., et al. 2013, ApJS, 207, 24
- Helou, G., Soifer, B.T., & Rowan-Robinson, M. 1985, ApJ, 298, L7
- Holland, W. S., Bintley, D., Chapin, E. L., et al. 2013, MNRAS, 430, 2513
- Holland, W. S., Robson, E. I., Gear, W. K., et al. 1999, MNRAS, 303, 659
- Hsu, L.-Y., Cowie, L. L., Chen, C.-C., Barger, A. J., & Wang, W.-H. 2016, ApJ, 829, 25
- Hughes, D. H., Serjeant, S., Dunlop, J., et al. 1998, Nature, 394, 241
- Ibar, E., Ivison, R. J., Beset, P. N., et al. 2010, MNRAS, 401, L53
- Inami, H., Bacon, R., Brinchmann, J., et al. 2017, A&A, 608, A2
- Jones, L., Rosenthal, M. J., Barger, A. J., & Cowie, L. L. 2021, ApJ, 916, 46
- Karim, A., Swinbank, M., Hodge, J., et al. 2013, MNRAS, 432, 2
- Kennicutt, R. C., Jr. 1998, ARA&A, 36, 189
- Klaas, U., Haas, M., Heinrichsen, I., & Schulz, B. 1997, A&A, 325, L21
- Koekemoer, A. M., Faber, S. M., Ferguson, H. C., et al. 2011, ApJS, 197, 36
- Kroupa, P. 2001, MNRAS, 322, 231
- Kurk, J., Cimatti, A., Daddi, E., et al. 2013, A&A, 549, A63
- Leitherer, C., Schaerer, D., Goldader, J. D., et al. 1999, ApJS, 123, 3
- Lim, C.-F., Wang, W.-H., Smail, I., et al. 2020, ApJ, 889, 80
- Luo, B., Brandt, W. N., Xue, Y. Q., et al. 2017, ApJS, 228, 2
- Madau, P., & Dickinson, M. 2014, ARA&A, 52, 415
- Magnelli, B., Popesso, P., Berta, S., et al. 2013, A&A, 553, 132
- Miller, N. A., Fomalont, E. B., Kellermann, K. I., et al. 2008, ApJ, 179, 114
- Momcheva, I. G., Brammer, G. V., van Dokkum, P. G., et al. 2016, ApJS, 225, 27
- Morrison, G. E., Owen, F. N., Dickinson, M., Ivison, R. J., & Ibar, E. 2010, ApJ, 188, 178
- Murphy, E. J., Condon, J. J., Schinnerer, E., et al. 2011, ApJ, 737, 67
- Owen, F. N. 2018, ApJS, 235, 34
- Pope, A., Chary, R.-R., Alexander, D. M., et al. 2008, ApJ, 675, 1171
- Popesso, P., Dickinson, M., Nonino, M., et al. 2009, A&A, 494, 443
- Reddy, N. A., Steidel, C. C., Erb, D. K., Shapley, A. E., & Pettini, M. 2006, ApJ, 653, 1004
- Reuter, C., Vieira, J. D., Spilker, J. S., et al. 2020, ApJ, 902, 78
- Salpeter, E. E. 1955, ApJ, 121, 161
- Santini, P., Ferguson, H. C., Fontana, A., et al. 2015, ApJ, 801, 97
- Schreiber, C., Elbaz, D., Pannella, M., et al. 2018, A&A, 609, 30
- Serjeant, S., Dunlop, J. S., Mann, R. G., et al. 2003, MNRAS, 344, 887
- Smail, I., Ivison, R. J., Blain, A. W. 1997, ApJL, 490, L5
- Smail, I., Ivison, R. J., Owen, F. N., Blain, A. W., & Kneib, J.-P. 2000, ApJ, 528, 612
- Stach, S. M., Dudzevičiūtė, U., Smail, I., et al. 2019, MNRAS, 487, 4648
- Straatman, C. M. S., Spitler, L. R., Quadri, R. F., et al. 2016, ApJ, 830, 51
- Swinbank, A. M., Simpson, J. M., Smail, I., et al. 2014, MNRAS, 438, 1267
- Swinbank, A. M., Smail, I., Chapman, S. C., et al. 2004, ApJ, 617, 64
- Szokoly, G. P., Bergeron, J., Hasinger, G., et al. 2004, ApJS, 155, 271
- Thomson, A. P., Ivison, R. J., Simpson, J. M., et al. 2014, MNRAS, 442, 577
- Treu, T., Ellis, R. S., Liao, T. X., et al. 2005, ApJL, 622, L5
- Trouille, L., Barger, A. J., Cowie, L. L., Yang, Y., & Mushotzky, R. F. 2008, ApJ, 179, 1
- Walter, F., Decarli, R., Carilli, C., et al. 2012, Natur, 486, 233
- Wang, T., Schreiber, C., Elbaz, D., et al. 2019, Natur, 572, 211
- Wang, W.-H., Lin, W.-C., Lim, C.-F., et al. 2017, ApJ, 850, 37
- Wardlow, J. L., Smail, I., Coppin, K. E. K., et al. 2011, MNRAS, 415, 1479
- Wirth, G. D., Trump, J. R., Barro, G., et al. 2015, AJ, 150, 153
- Wirth, G. D., Willmer, C. N. A., Amico, P., et al. 2004, AJ, 127, 3121
- Yang, G., Xue, Y. Q., Luo, B., et al. 2014, ApJS, 215, 27
- Zavala, J. A., Aretxaga, I., Dunlop, J. S., et al. 2018, MNRAS, 475, 5585
- Zavala, J. A., Aretxaga, I., Geach, J. E., et al. 2017, MNRAS, 464, 3369

Table 2. CDF-N SCUBA-2 450 μ m Sample ($> 4\sigma$)

No. and Name	R.A. ⁴⁵⁰	Decl.	450 μ m	SNR	R.A. ^{VLA}	Decl.	20 cm	850 μ m	z	offset
	(J2000.0)		(mJy)		(J2000.0)		(μ Jy)	(mJy)		($''$)
(1)	(2)	(3)	(4)	(5)	(6)	(7)	(8)	(9)	(10)	(11)
1 SMM023730-621300	12 37 30.62	62 13 0.09	32.3(2.20)	14.64	12 37 30.80	62 12 58.7	123(6.1)	12.60(0.26)	2.88	1.82
2 SMM023537-622239	12 35 37.82	62 22 39.2	28.6(4.38)	6.52	12 35 38.15	62 22 41.0	154(8.6)	3.93(0.53)	1.23	3.01
3 SMM023546-622012	12 35 46.80	62 20 12.5	25.5(3.91)	6.53	12 35 46.66	62 20 13.4	46(6.8)	10.79(0.50)	3.132	1.32
4 SMM023707-621408	12 37 7.309	62 14 8.29	24.4(1.69)	14.36	12 37 7.210	62 14 8.19	59(8.7)	7.95(0.20)	3.06	1.46
5 SMM023721-620709	12 37 21.09	62 07 9.20	25.1(4.02)	6.24	12 37 21.40	62 07 8.30	293(9.3)	4.85(0.52)	2.17	2.36
6 SMM023711-621330	12 37 11.31	62 13 30.2	25.5(1.71)	14.90	12 37 11.34	62 13 30.9	126(6.3)	8.71(0.20)	1.995	0.73
7 SMM023618-621549	12 36 18.48	62 15 49.2	23.4(2.40)	9.76	12 36 18.35	62 15 50.4	169(7.7)	7.53(0.28)	1.865	1.60
8 SMM023701-621145	12 37 1.442	62 11 45.4	22.6(1.51)	14.92	12 37 1.578	62 11 46.4	95(5.7)	6.55(0.19)	1.760	1.42
9 SMM023527-622218	12 35 27.34	62 22 18.7	22.7(5.02)	4.51	off radio	2.49(0.64)	2.71	...
10 SMM023610-622042	12 36 10.05	62 20 42.9	21.9(4.25)	5.14	12 36 9.880	62 20 45.5	149(20.5)	5.20(0.53)	0.6309	2.81
11 SMM023623-622009	12 36 23.01	62 20 9.19	21.2(4.66)	4.55	12 36 23.05	62 20 7.90	51(7.6)	3.09(0.56)	1.98	1.34
12 SMM023622-621628	12 36 22.78	62 16 28.2	19.9(2.36)	8.42	12 36 22.67	62 16 29.7	81(7.8)	3.03(0.27)	1.790	1.74
13 SMM023556-622236	12 35 56.21	62 22 36.7	19.7(3.56)	5.54	12 35 55.90	62 22 39.0	56(7.9)	11.74(0.44)	3.148	3.20
14 SMM023558-621353	12 35 58.21	62 13 53.7	20.2(4.47)	4.51	12 35 58.19	62 13 53.9	75(16.1)	1.10(0.45)	...	1.62
15 SMM023551-622144	12 35 51.65	62 21 44.5	19.1(3.39)	5.65	12 35 51.40	62 21 47.2	51(7.3)	18.84(0.43)	4.422	3.17
16 SMM023629-621048	12 36 29.28	62 10 48.3	17.6(1.99)	8.87	12 36 29.03	62 10 45.5	91(7.1)	1.60(0.26)	1.013	3.25
17 SMM023645-621448	12 36 45.99	62 14 48.4	18.4(1.71)	10.74	12 36 46.08	62 14 48.6	103(3.7)	5.63(0.20)	2.94	0.65
18 SMM023616-621515	12 36 16.21	62 15 15.0	19.4(2.38)	8.17	12 36 16.10	62 15 13.7	38(2.9)	5.60(0.28)	2.578	1.54
19 SMM023635-621423	12 36 35.84	62 14 23.2	18.0(1.88)	9.53	12 36 35.59	62 14 24.0	78(5.1)	4.35(0.22)	2.005	1.86
20 SMM023634-621242	12 36 34.84	62 12 42.3	17.7(1.68)	10.55	12 36 34.51	62 12 40.9	188(7.7)	1.48(0.21)	1.224	2.65
21 SMM023735-621057	12 37 35.43	62 10 57.9	16.5(2.58)	6.39	12 37 35.55	62 10 55.9	32(5.8)	2.51(0.31)	1.141	2.15
22 SMM023713-621824	12 37 13.53	62 18 24.2	16.7(3.05)	5.47	12 37 13.89	62 18 26.2	623(19.4)	5.45(0.33)	...	3.21
23 SMM023709-620841	12 37 9.700	62 08 41.3	17.1(2.17)	7.87	12 37 9.748	62 08 41.2	156(6.9)	3.34(0.28)	0.9021	0.37
24 SMM023544-622241	12 35 44.85	62 22 41.4	16.9(3.81)	4.45	12 35 44.82	62 22 42.2	61(8.2)	4.61(0.47)	1.54	0.90
25 SMM023603-621113	12 36 3.142	62 11 13.9	17.2(3.33)	5.17	12 36 3.262	62 11 10.9	142(6.6)	1.11(0.41)	0.6380	3.12
26 SMM023633-621407	12 36 33.39	62 14 7.29	17.2(1.89)	9.14	12 36 33.42	62 14 8.50	33(5.4)	9.56(0.23)	5.302	1.19
27 SMM023635-621922	12 36 35.07	62 19 22.2	17.5(3.95)	4.42	12 36 34.92	62 19 23.5	81(4.5)	6.00(0.44)	...	1.59
28 SMM023646-620834	12 36 46.72	62 08 34.4	17.0(2.02)	8.43	12 36 46.68	62 08 33.2	95(5.8)	2.31(0.28)	0.9710	1.15
29 SMM023700-620909	12 37 0.428	62 09 9.41	16.5(1.93)	8.56	12 37 0.270	62 09 9.70	297(10.1)	3.68(0.26)	1.61	1.14
30 SMM023725-620858	12 37 25.10	62 08 58.0	15.0(2.55)	5.90	12 37 25.00	62 08 56.5	84(7.3)	2.94(0.33)	0.9367	1.78
31 SMM023631-620958	12 36 31.28	62 09 58.3	15.2(2.06)	7.40	12 36 31.26	62 09 57.6	140(3.8)	3.97(0.28)	2.313	0.64
32 SMM023741-621220	12 37 41.61	62 12 20.7	14.6(2.96)	4.96	12 37 41.70	62 12 23.7	18(3.0)	3.61(0.34)	2.90	2.95
33 SMM023628-620713	12 36 28.05	62 07 13.3	13.7(3.38)	4.07	0.870(0.43)	1.35	...
34 SMM023726-620824	12 37 26.39	62 08 24.0	14.1(2.93)	4.83	12 37 26.66	62 08 23.2	51(5.4)	3.61(0.38)	2.10	2.08

Table 2 *continued*

Table 2 (*continued*)

No. and Name	R.A. ⁴⁵⁰ (J2000.0)	Decl. (J2000.0)	450 μ m (mJy)	SNR	R.A. VLA (J2000.0)	Decl. (J2000.0)	20 cm (μ Jy)	850 μ m (mJy)	z	offset ($''$)
(1)	(2)	(3)	(4)	(5)	(6)	(7)	(8)	(9)	(10)	(11)
35 SMM023658-620931	12 36 58.42	62 09 31.4	12.8(1.88)	6.83	12 36 58.55	62 09 31.4	28(2.7)	4.46(0.25)	contam.	0.92
36 SMM023716-621642	12 37 16.36	62 16 42.2	13.4(2.31)	5.79	12 37 16.62	62 16 43.4	80(3.9)	2.77(0.25)	0.5573	2.14
37 SMM023618-621408	12 36 18.09	62 14 8.08	13.3(2.13)	6.23	12 36 17.83	62 14 7.91	14(2.5)	1.99(0.27)	0.8460	1.83
38 SMM023706-620723	12 37 6.536	62 07 23.2	12.4(2.75)	4.50	12 37 6.807	62 07 22.2	86(6.6)	0.914(0.37)	1.218	2.10
39 SMM023730-621617	12 37 30.97	62 16 17.0	12.6(2.76)	4.57	12 37 31.20	62 16 20.2	65(3.9)	1.69(0.30)	0.9750	3.55
40 SMM023719-621022	12 37 19.42	62 10 22.1	12.8(2.15)	5.94	12 37 19.55	62 10 21.2	22(2.7)	3.94(0.27)	...	1.35
41 SMM023637-620853	12 36 37.02	62 08 53.3	13.1(2.06)	6.34	12 36 37.03	62 08 52.4	90(5.4)	3.70(0.29)	2.05	1.00
42 SMM023712-621035	12 37 12.42	62 10 35.2	11.1(2.04)	5.43	12 37 12.48	62 10 35.6	21(2.7)	5.40(0.26)	...	0.48
43 SMM023622-621615	12 36 22.21	62 16 15.2	12.7(2.35)	5.41	12 36 22.10	62 16 15.9	20(2.8)	3.08(0.27)	...	0.99
44 SMM023631-621716	12 36 31.92	62 17 16.2	11.7(2.33)	5.02	12 36 31.94	62 17 14.7	22(2.8)	8.54(0.26)	3.36	1.59
45 SMM023633-621006	12 36 33.59	62 10 6.29	12.2(2.03)	6.01	12 36 33.69	62 10 5.79	50(6.0)	0.927(0.28)	1.016	0.88
46 SMM023621-621710	12 36 21.32	62 17 10.2	12.2(2.63)	4.64	12 36 21.28	62 17 8.40	148(4.1)	4.92(0.29)	1.988	1.81
47 SMM023717-620803	12 37 17.39	62 08 3.20	11.0(2.65)	4.15	12 37 17.46	62 08 4.40	32(5.7)	4.26(0.35)	1.42	1.28
48 SMM023611-621033	12 36 11.72	62 10 33.0	11.1(2.53)	4.37	12 36 11.52	62 10 33.5	21(2.7)	2.38(0.33)	2.35	1.55
49 SMM023619-621006	12 36 19.44	62 10 6.19	10.4(2.26)	4.63	12 36 19.11	62 10 4.30	29(2.8)	2.68(0.30)	2.11	2.99
50 SMM023637-621156	12 36 37.13	62 11 56.4	10.4(1.67)	6.25	4.43(0.22)	3.27	...
51 SMM023702-621301	12 37 2.307	62 13 1.40	11.6(1.42)	8.13	12 37 2.570	62 13 2.40	29(2.7)	2.56(0.18)	...	2.09
52 SMM023612-621146	12 36 12.55	62 11 46.0	11.2(2.29)	4.89	1.95(0.30)	0.29	...
53 SMM023634-620943	12 36 34.87	62 09 43.2	12.4(2.03)	6.10	3.69(0.28)	2.10	...
54 SMM023608-621249	12 36 8.961	62 12 49.0	10.3(2.49)	4.15	12 36 8.671	62 12 51.0	42(6.1)	2.51(0.31)	...	2.83
55 SMM023730-621254	12 37 30.47	62 12 54.0	10.1(2.19)	4.63	blend(1)
56 SMM023702-621401	12 37 2.600	62 14 1.40	9.74(1.54)	6.32	12 37 2.761	62 14 1.70	17(2.6)	1.96(0.19)	1.248	1.18
57 SMM023712-621212	12 37 12.16	62 12 12.2	8.88(1.78)	4.97	12 37 12.05	62 12 11.9	32(2.7)	3.94(0.22)	2.914	0.86
58 SMM023655-620808	12 36 55.00	62 08 8.41	8.53(2.14)	3.98	2.53(0.29)
59 SMM023713-621543	12 37 13.34	62 15 43.2	9.56(2.20)	4.33	12 37 13.69	62 15 44.4	29(7.3)	2.61(0.24)	2.300	2.72
60 SMM023629-621515	12 36 29.67	62 15 15.2	8.98(2.13)	4.21	12 36 29.45	62 15 13.1	14(2.5)	2.28(0.25)	3.652	2.59
61 SMM023652-621227	12 36 52.01	62 12 27.3	8.73(1.35)	6.45	12 36 52.03	62 12 25.9	12(2.4)	6.10(0.17)	5.183	1.51
62 SMM023718-621135	12 37 18.28	62 11 35.2	8.18(2.03)	4.02	12 37 18.24	62 11 33.0	23(2.6)	1.99(0.26)	1.013	2.11
63 SMM023642-621544	12 36 42.40	62 15 44.4	8.78(1.97)	4.45	12 36 42.22	62 15 45.4	185(7.2)	1.98(0.22)	0.8575	1.66
64 SMM023720-621247	12 37 20.60	62 12 47.2	8.95(1.95)	4.58	1.25(0.24)	contam.	...
65 SMM023653-620848	12 36 53.71	62 08 48.4	8.63(1.94)	4.43	12 36 53.60	62 08 49.9	20(2.5)	1.65(0.27)	2.41	1.69
66 SMM023659-621449	12 36 59.02	62 14 49.4	8.28(1.70)	4.85	3.51(0.20)
67 SMM023711-621324	12 37 11.75	62 13 24.2	8.51(1.72)	4.94	12 37 12.00	62 13 25.7	55(5.1)	blend(6)	1.996	2.31
68 SMM023636-621436	12 36 36.11	62 14 36.2	8.98(1.92)	4.67	12 36 35.89	62 14 36.0	32(2.7)	1.18(0.23)	1.018	1.57
69 SMM023638-621112	12 36 38.01	62 11 12.4	8.40(1.79)	4.68	1.41(0.24)	0.98	...
70 SMM023648-621217	12 36 48.71	62 12 17.4	8.40(1.38)	6.06	12 36 48.65	62 12 15.7	22(2.7)	1.80(0.18)	1.066	1.67

Table 2 *continued*

Table 2 (*continued*)

No. and Name	R.A. ⁴⁵⁰ (J2000.0)	Decl. (J2000.0)	450 μ m (mJy)	SNR	R.A. VLA (J2000.0)	Decl. (J2000.0)	20 cm (μ Jy)	850 μ m (mJy)	z	offset ($''$)
(1)	(2)	(3)	(4)	(5)	(6)	(7)	(8)	(9)	(10)	(11)
71 SMM023634-621212	12 36 34.55	62 12 12.2	8.17(1.71)	4.77	12 36 34.47	62 12 12.9	221(8.5)	0.142(0.22)	0.4575	0.90
72 SMM023713-621157	12 37 13.87	62 11 57.2	7.64(1.87)	4.07	12 37 14.05	62 11 56.5	21(2.6)	3.62(0.24)	4.59	1.41
73 SMM023634-621359	12 36 34.54	62 13 59.3	7.91(1.83)	4.30	12 36 34.28	62 14 0.59	36(5.3)	1.77(0.22)	1.38	2.20
74 SMM023635-621155	12 36 35.99	62 11 55.2	7.49(1.70)	4.38	12 36 36.13	62 11 54.4	21(5.7)	4.43(0.22)	3.91	1.22
75 SMM023645-621146	12 36 45.85	62 11 46.4	7.30(1.48)	4.90	0.177(0.19)
76 SMM023653-621137	12 36 53.14	62 11 37.4	6.43(1.46)	4.39	12 36 53.37	62 11 39.5	74(7.6)	1.31(0.19)	1.269	2.72
77 SMM023639-621255	12 36 39.42	62 12 55.4	7.12(1.54)	4.61	12 36 38.89	62 12 56.9	27(6.9)	0.861(0.20)	1.144	3.97
78 SMM023656-621204	12 36 56.28	62 12 4.41	6.49(1.40)	4.61	12 36 56.59	62 12 7.40	38(5.2)	3.86(0.18)	0.29	3.64
79 SMM023649-621314	12 36 49.71	62 13 14.4	5.59(1.37)	4.06	12 36 49.73	62 13 12.9	57(5.0)	0.834(0.17)	0.4750	1.41

NOTE—The columns are (1) the SCUBA-2 450 μ m source number and name, (2 and 3) the SCUBA-2 450 μ m R.A. and Decl., (4) the 450 μ m flux and, in parentheses, the error; these were measured from the SCUBA-2 matched-filter image, (5) the SNR from the 450 μ m measurements, (6 and 7) the accurate R.A. and Decl. of the corresponding VLA 20 cm source, when available, (8) the VLA 20 cm flux and, in parentheses, the error; these come from Owen (2018), unless marked with an “a”, in which case they come from Morrison et al. (2010), (9) the SCUBA-2 850 μ m flux and, in parentheses, error; these were measured at the 450 μ m position, though note that two of the 450 μ m sources are blended at 850 μ m, so these are labeled “blend” with the number in parentheses giving the 450 μ m source number of the brighter source in the pair to whom we assigned all of the measured 850 μ m flux, (10) the specz (three significant figures after the decimal point; see Section 2.6 for references, except for those marked with a “b”, which are NOEMA redshifts from Jones et al. 2021), or the photz (two significant figures after the decimal point) from Momcheva et al. (2016), where available, then Yang et al. (2014); some sources have neither, and two sources are marked “contam.”, because the photometry is contaminated by a neighboring star or galaxy, and (11) the offset between the SCUBA-2 450 μ m and VLA source positions.

Table 3. CDF-S SCUBA-2 450 μ m Sample ($> 4\sigma$)

No. and Name	R.A. ⁴⁵⁰	Decl.	450 μ m	SNR	R.A. ^{ALMA}	Decl.	850 μ m	20 cm	850 μ m	z	offset
(1)	(2)	(3)	(4)	(5)	(6)	(7)	(8)	(9)	(10)	(11)	(12)
1 SMM033204-274647	3 32 4.950	-27 46 47.2	27.0(4.6)	5.8	3 32 4.889	-27 46 47.7	6.45	130	7.7(0.38)	2.252	0.94
2 SMM033248-274934	3 32 48.52	-27 49 34.2	19.7(4.4)	4.4	3 32 48.55	-27 49 34.7	...	135	2.6(0.38)	1.120	0.64
3 SMM033249-274917	3 32 49.11	-27 49 17.2	19.5(4.5)	4.3	blend(2)
4 SMM033207-275119	3 32 7.349	-27 51 19.2	19.2(4.7)	4.0	3 32 7.289	-27 51 20.8	8.93	120	3.3(0.36)	contam.	1.87
5 SMM033219-274603	3 32 19.57	-27 46 3.29	18.7(3.2)	5.8	3 32 19.70	-27 46 2.20	4.90	51	3.7(0.30)	2.41	2.03
6 SMM033235-274917	3 32 35.70	-27 49 17.2	18.0(3.1)	5.7	3 32 35.73	-27 49 16.2	5.09	80	4.7(0.27)	2.576	1.16
7 SMM033215-275037	3 32 15.49	-27 50 37.2	17.2(3.4)	4.9	3 32 15.33	-27 50 37.6	6.61	50	4.6(0.28)	3.12	2.26
8 SMM033222-274935	3 32 22.42	-27 49 35.2	15.3(2.6)	5.8	3 32 22.47	-27 49 35.2	0.934	77	3.8(0.24)	0.7323	0.67
9 SMM033222-274807	3 32 22.28	-27 48 7.29	14.6(2.5)	5.7	3 32 22.28	-27 48 4.79	5.21	42	6.1(0.23)	3.847	2.49
10 SMM033232-274545	3 32 32.53	-27 45 45.2	14.6(3.3)	4.3	near edge	...	2.9(0.33)
11 SMM033243-274639	3 32 43.53	-27 46 39.2	14.4(3.4)	4.2	3 32 43.53	-27 46 39.2	3.18	...	4.7(0.34)	2.794	0.0
12 SMM033238-274633	3 32 38.41	-27 46 33.2	13.9(3.0)	4.5	3 32 38.55	-27 46 34.5	2.04	...	2.2(0.31)	2.543	2.32
13 SMM033228-275041	3 32 28.16	-27 50 41.2	12.9(3.2)	4.0	0.76(0.28)
14 SMM033228-274659	3 32 28.46	-27 46 59.2	12.9(2.6)	4.8	3 32 28.50	-27 46 58.3	6.39	103	4.8(0.26)	2.309	1.11
15 SMM033234-274940	3 32 34.33	-27 49 40.2	12.5(3.0)	4.0	3 32 34.27	-27 49 40.3	4.73	...	4.8(0.27)	3.76	0.92
16 SMM033228-274827	3 32 28.75	-27 48 27.2	9.65(2.3)	4.0	3 32 28.80	-27 48 29.7	1.57	...	2.0(0.23)	1.83	2.58

NOTE—The columns are (1) the SCUBA-2 450 μ m source number and name, (2 and 3) the SCUBA-2 450 μ m R.A. and Decl., (4) the 450 μ m flux and, in parentheses, the error; these were measured from the SCUBA-2 matched-filter image, (5) the SNR from the 450 μ m measurements, (6 and 7) the accurate R.A. and Decl. of the corresponding ALMA 870 μ m source, when available (for source 2, it is the VLA 20 cm source position), (8) the ALMA 850 μ m flux, (9) the VLA 20 cm flux from Miller et al. (2008), (10) the SCUBA-2 850 μ m flux and, in parentheses, error; these were measured at the position of the 450 μ m source when there is no ALMA 870 μ m position, though note that one of the 450 μ m sources is blended at 850 μ m, so it is labeled “blend” with the number in parentheses giving the 450 μ m source number of the brighter source in the pair to whom we assigned all of the measured 850 μ m flux, (11) the specz (three significant figures after the decimal point; see Section 2.6 for references) or the photz (two significant figures after the decimal point; Straatman et al. 2016); some sources have neither, and one source is marked “contam.”, because the ALMA position places the source at the edge of another source (see bottom-left thumbnail of Figure 9), and (12) the offset between the SCUBA-2 450 μ m and ALMA source positions, except for source 2, where the offset is between the SCUBA-2 450 μ m and VLA source positions.

Table 4. High-Redshift Submillimeter Galaxies

No. and Name	450 μ m (mJy)	850 μ m (mJy)	20 cm (mJy)	20 cm/850 μ m ($\times 10^{-3}$)	450 μ m/850 μ m	z (from Table 2)	$z_{20/850}$	$z_{450/850}$
(1)	(2)	(3)	(4)	(5)	(6)	(7)	(8)	(9)
High-Redshift Candidates Based on the Criteria of Figure 7								
GN-1 SMM023730-621300	32.3	12.60	123	9.78	2.58	2.88	...	3.38
GN-27 SMM023635-621922	17.5	6.00	81	13.63	2.78	3.18
GN-42 SMM023712-621035	11.1	5.40	21	4.05	2.33	...	4.31	3.66
GN-44 SMM023631-621716	11.7	8.54	22	2.57	1.46	3.36	5.03	4.91
GN-47 SMM023717-620803	11.0	4.26	32	7.59	2.76	3.20
GN-50 SMM023637-621156	10.4	4.43	< 11	< 2.48	2.56	3.27	> 5.09	3.40
GN-53 SMM023634-620943	12.4	3.69	< 11	< 2.97	2.95	...	> 4.80	3.02
GN-58 SMM023655-620808	8.53	2.53	< 11	< 4.33	3.82	...	> 4.20	...
GN-66 SMM023659-621449	8.28	3.51	< 11	< 3.13	2.47	...	> 4.72	3.50
GN-72 SMM023713-621157	7.64	3.62	21	5.96	2.18	4.59	...	3.84
GN-74 SMM023635-621155	7.49	4.43	21	4.80	1.66	3.91	4.04	4.57
GN-78 SMM023656-621204	6.49	3.86	38	10.02	1.64	4.60
Additional Photometric High-Redshift Candidates								
GN-4 SMM023707-621408	24.4	7.95	59	7.47	3.18	3.06		
GS-7 SMM033215-275037	17.2	6.61	50	10.77	3.69	3.12		
GS-15 SMM033234-274940	12.5	4.73	< 29	< 6.02	2.60	3.76		
Spectroscopic High-Redshift Galaxies								
GN-3 SMM023546-622012	25.5	10.79	46	4.28	2.35	3.132		
GN-13 SMM023556-622236	19.7	11.74	56	4.81	1.67	3.148		
GN-15 SMM023551-622144	19.1	18.84	51	2.75	1.02	4.422		
GN-26 SMM023633-621407	17.2	9.56	33	3.45	16.87	5.302		
GN-60 SMM023629-621515	8.98	2.28	14	6.2	9.42	3.652		
GN-61 SMM023652-621227	8.73	6.10	12	1.96	1.54	5.183		
GS-9 SMM033222-274807	14.6	5.21	42	6.8	14.69	3.847		